RSC Advances

PAPER

View Article Online
View Journal | View Issue

Cite this: *RSC Adv.*, 2026, **16**, 27560

A layered double hydroxide nanocarrier enables YM155 delivery-induced PANoptosis and immunogenic activation in hepatocellular carcinoma

Jie Gong,[abcd] Xianxing Wang,[cd] Jiali Yang,[cd] Li Tang,*[cd] Lei Cai*[cd] and Huaizhi Wang*[acd]

Hepatocellular carcinoma (HCC) remains a highly lethal malignancy due to its intrinsic resistance to apoptosis and limited response to conventional chemotherapy. This therapeutic bottleneck is closely associated with aberrant cell death regulation and an immunosuppressive tumor microenvironment, which collectively restrict effective tumor eradication. In this study, a layered double hydroxide (LDH)-based YM155 delivery platform (LDH-YM155) is developed to enhance Survivin-targeted therapy while simultaneously reprogramming tumor cell death toward an inflammatory and immunogenic phenotype. LDH-YM155 exhibits favorable physicochemical stability, pH-responsive YM155 release, and efficient cellular internalization, triggering pronounced oxidative stress and mitochondrial membrane depolarization in Hepa1-6 cells. This stress cascade activates PANoptosis characterized by elevated caspase-3, caspase-8 and caspase-1 activity, ASC speck formation, elevated p-MLKL levels, increased Annexin V/PI-positive populations, and upregulated NLRP3 and RIPK3 signaling. In parallel, LDH-YM155 induces immunogenic cell death-associated events, including enhanced calreticulin exposure, extracellular HMGB1 and ATP release, and increased lactate dehydrogenase release, thereby promoting dendritic cell maturation through tumor cell-conditioned media. Transcriptomic profiling further confirms activation of stimulus-responsive and inflammatory signaling pathways consistent with the observed phenotype. *In vivo*, LDH-YM155 demonstrates improved tumor accumulation and significantly suppresses tumor growth in a Hepa1-6 tumor-bearing mouse model, accompanied by reduced Ki-67 expression and increased TUNEL staining. Importantly, tumor tissue staining validates elevated NLRP3, RIPK3, and CRT signals with reduced HMGB1 retention, supporting the induction of inflammatory and immunogenic tumor cell death *in vivo*. Further immune profiling revealed enhanced dendritic cell maturation, pro-inflammatory macrophage polarization, and increased cytotoxic $CD8^+$Granzyme B^+ T-cell activation within the tumor microenvironment. Collectively, this LDH-based nanotherapeutic strategy enhances YM155 efficacy by coupling Survivin inhibition with PANoptosis activation and ICD-associated immune stimulation, providing a promising platform for hepatocellular carcinoma therapy.

Received 16th February 2026
Accepted 6th May 2026

DOI: 10.1039/d6ra01379a

rsc.li/rsc-advances

1 Introduction

Hepatocellular carcinoma (HCC) remains one of the leading causes of cancer-related deaths worldwide, with the highest burden seen in regions where hepatitis virus infections are endemic, such as Asia and sub-Saharan Africa.[1–3] Although diagnostic tools and treatments like molecular targeted agents and immune checkpoint inhibitors have advanced over the years, most patients still present at a stage where curative options are no longer feasible.[4,5] Consequently, recurrence rates stay high and long-term survival remains disappointingly low.[6]

A major reason behind this therapeutic failure lies in how HCC cells to evade programmed cell death. When apoptosis is dysregulated, cancer cells become resilient to metabolic stress, DNA damage, and various treatments, essentially giving them a free pass to keep growing and resisting therapy.[7] At the heart of this evasion is Survivin, a protein encoded by the BIRC5 gene.[8] As a member of the inhibitor of apoptosis protein (IAP) family, Survivin steps in to block caspase activation and helps keep mitosis on track, which in turn supports both cell survival

[a]*Chongqing Medical University, Chongqing 400044, P. R. China. E-mail: whuaizhi@gmail.com*
[b]*Chongqing School, University of Chinese Academy of Sciences, Chongqing 400044, P. R. China*
[c]*Chongqing General Hospital, Chongqing University, Chongqing 400044, P. R. China. E-mail: 284753883@qq.com; cailei@rocketmail.com*
[d]*Chongqing Key Laboratory of Intelligent Medicine Engineering for Hepatopancreatobiliary Diseases, Chongqing 400044, P. R. China*

and proliferation.[9] What makes Survivin particularly relevant is its expression pattern: it shows up at high levels in HCC and many other cancers, but stays mostly quiet in normal adult tissues.[10] Clinically, this expression pattern is important because elevated Survivin has been associated with tumor aggressiveness, poor prognosis, and resistance to chemotherapy and radiotherapy.[11–13]

YM155 is a small-molecule compound reported to suppress Survivin expression at the transcriptional level.[14] Preclinical studies have demonstrated that YM155 can sensitize tumor cells to apoptosis and inhibit tumor growth across multiple cancer models.[15–18] However, its clinical application has been limited by unfavorable pharmacokinetic properties, including rapid systemic clearance, poor bioavailability, and insufficient tumor accumulation. These limitations restrict its therapeutic window and underscore the need for effective delivery strategies to enhance intratumoral drug exposure while reducing off-target effects.

Although YM155 is widely recognized as a pro-apoptotic agent through Survivin suppression, accumulating studies suggest that apoptosis alone does not fully account for therapy-induced tumor cell elimination, particularly under conditions of severe intracellular stress or in apoptosis-resistant tumors. Recent evidence suggests that tumor cell death induced by anticancer therapies often extends beyond classical apoptosis and may involve multiple regulated cell death pathways.[19,20] In particular, therapies that induce oxidative stress, mitochondrial dysfunction, or membrane damage may concurrently activate multiple death-related signaling modules, resulting in mixed or integrated regulated cell death phenotypes. In this context, the concept of PANoptosis has been proposed to describe a coordinated cell death program integrating apoptotic, pyroptotic, and necroptotic signaling.[21,22] Unlike apoptosis alone, these interconnected pathways are frequently associated with membrane disruption and inflammatory responses.[23] Such features are of particular relevance in apoptosis-resistant tumors, where activation of alternative death mechanisms may enhance therapeutic efficacy.

In parallel, increasing attention has been directed toward the immunological consequences of tumor cell death. Notably, regulated cell death programs involving membrane permeabilization and inflammatory signaling, such as PANoptosis, are increasingly recognized as potential drivers of immunogenic cell death (ICD), as they facilitate the release and exposure of danger-associated molecular patterns (DAMPs) during tumor cell demise.[24] ICD is characterized by the surface translocation of calreticulin and the release of HMGB1, which together promote antigen uptake, dendritic cell maturation, and subsequent activation of tumor-specific adaptive immunity.[25,26] These immune-stimulatory events are particularly relevant in apoptosis-resistant tumors, where engaging inflammatory cell death pathways may not only enhance direct cytotoxicity but

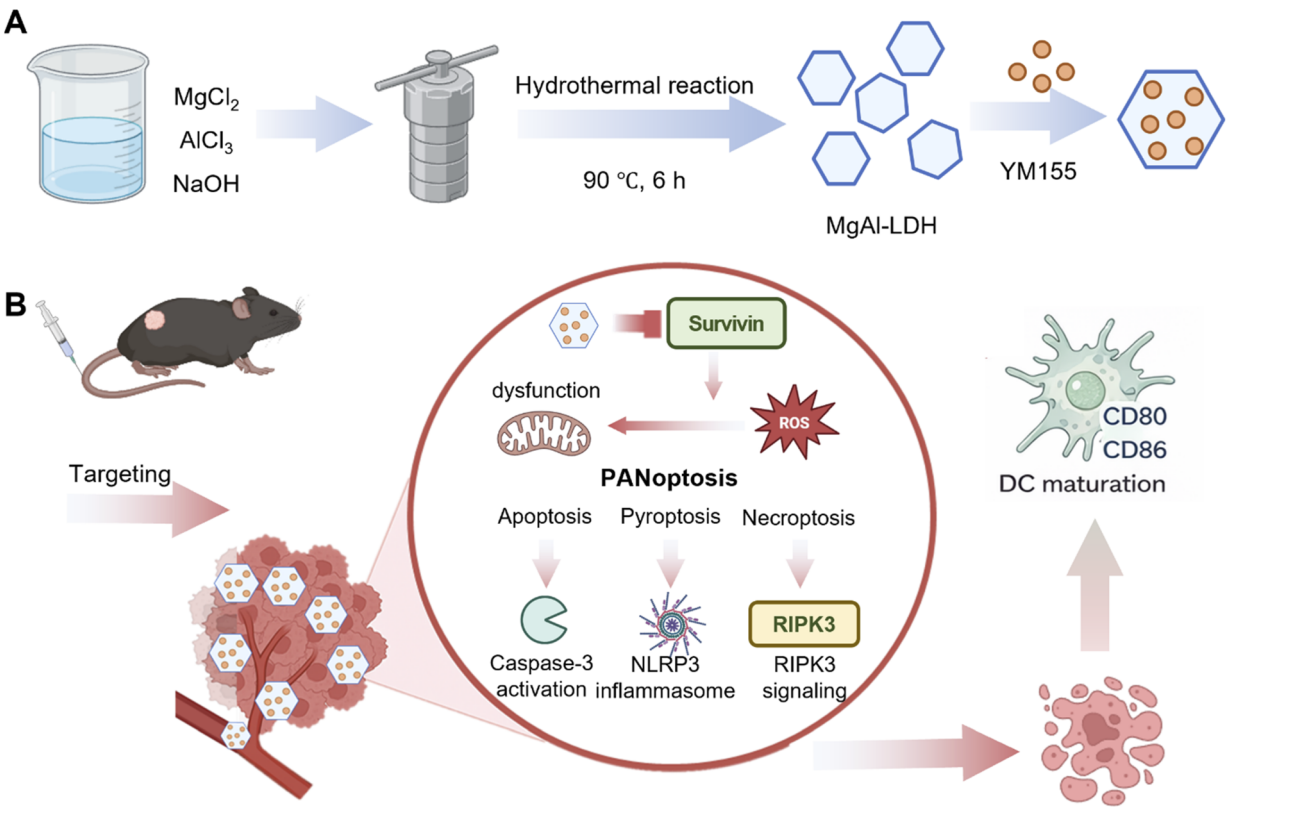

Fig. 1 Schematic illustration of LDH-YM155 synthesis and its PANoptosis-related antitumor mechanism in HCC. (A) Preparation of MgAl-LDH nanosheets and YM155-loaded LDH-YM155 nanocomposites. (B) LDH-YM155 accumulates in tumor tissue, suppresses Survivin, induces ROS-mediated PANoptosis-related signaling, and promotes dendritic cell maturation.

also convert tumor cell death into an immunologically active process.[27] In HCC, where the tumor microenvironment is frequently immunosuppressive, therapeutic strategies capable of coupling PANoptosis with ICD-mediated immune activation are therefore of growing interest.

Nanocarrier-based drug delivery systems have emerged as effective tools to address pharmacological limitations of small-molecule anticancer agents.[28] Among them, layered double hydroxides (LDHs) have attracted attention due to their two-dimensional lamellar structure, tunable metal composition, high drug loading capacity, and pH-responsive release behavior.[29–31] LDHs feature positively charged metal hydroxide layers, with anions and water molecules sandwiched in between. This structure allows them to bind electrostatically with drug molecules that carry negative charges or are polar in nature.[32] These properties allow LDHs to improve drug stability, facilitate intracellular delivery, and enhance tumor accumulation *via* the enhanced permeability and retention effect.[33]

Although LDH-based nanocarriers have been explored for the delivery of chemotherapeutic agents and nucleic acids, their application in delivering pro-apoptotic small-molecule inhibitors such as YM155 remains relatively limited.[34,35] Given the dependence of HCC on Survivin-mediated survival signaling, an LDH-based delivery system capable of enhancing YM155 accumulation within tumor cells may effectively overcome apoptosis resistance.[36] Moreover, the intracellular stress responses triggered by LDH-mediated delivery may engage additional regulated cell death pathways and promote immunogenic features of tumor cell death.

In this study, we developed a MgAl-layered double hydroxide nanocomposite loaded with YM155 (LDH-YM155) to improve the therapeutic efficacy of Survivin inhibition in hepatocellular carcinoma. The physicochemical properties of LDH-YM155 were characterized, and its antitumor activity was evaluated *in vitro* and *in vivo*. We further investigated the mode of cell death induced by LDH-YM155, with a focus on the involvement of multiple regulated cell death pathways and ICD–associated signals. Biodistribution and biosafety analyses were also performed to assess its translational potential (Fig. 1).

2 Materials and methods

2.1 Preparation of LDH and LDH-YM155

A mixed metal salt solution was prepared by combining 2 mL of 150 mM magnesium chloride hexahydrate and 1.25 mL of 80 mM aluminum chloride hexahydrate with deionized water to a final volume of 10 mL, yielding concentrations of 30 mM Mg^{2+} and 10 mM Al^{3+}. Separately, 6 mL of 1 M sodium hydroxide solution was diluted with 34 mL of deionized water.

During synthesis, the metal salt solution was stirred at 500 rpm, while the diluted alkaline solution was added dropwise over a period of 90 minutes to promote controlled nucleation and growth of LDH. The resulting suspension put into an autoclave and hydrothermally treated at 90 °C for 6 hours.The product was centrifuged at 9000 rpm for 5 minutes, washed with deionized water, then recentrifuged. This washing procedure was repeated three times to remove residual ions and unreacted species. The obtained white precipitate was designated as MgAl LDH and used for subsequent experiments.

For preparation of the LDH-YM155 nanocomposite, 1 mg of lyophilized MgAl LDH powder was dispersed in 500 μL of double distilled water with gentle vortexing to ensure uniform suspension. Subsequently, 500 μL of YM155 solution (1 mg mL^{-1}) was added under mild stirring. The mixture incubated at 4 °C overnight to allow YM155 molecules to associate with the LDH matrix through electrostatic interactions and interlayer accommodation. After incubation, the suspension was centrifuged at 9000 rpm for 10 min, and the collected product was washed once with double distilled water to remove loosely bound drug molecules. The final LDH-YM155 product was redispersed for further characterization and biological evaluation.

The drug loading capacity and encapsulation efficiency of YM155 in LDH-YM155 were determined by measuring the amount of unloaded YM155 in the supernatant after centrifugation. Briefly, after YM155 loading, the suspension was centrifuged, and the supernatant containing unbound YM155 was collected. Before absorbance measurement, YM155-containing solutions were alkalized with 0.1 M NaOH, and the absorbance was measured at 450 nm. YM155 concentration was calculated according to a standard curve prepared under the same alkaline conditions. Drug loading capacity and encapsulation efficiency were calculated as follows: drug loading capacity (%) = weight of loaded YM155/weight of LDH-YM155 × 100%; encapsulation efficiency (%) = weight of loaded YM155/weight of initially added YM155 × 100%.

2.2 Characterization of LDH and LDH-YM155

The physicochemical properties of LDH and LDH-YM155 were characterized using multiple analytical techniques. For atomic force microscopy (AFM) analysis, approximately 5 μL of diluted sample suspension was deposited onto freshly cleaved mica substrates and dried under ambient conditions prior to imaging.

X-ray diffraction (XRD) measurements were performed using freeze dried samples that were finely ground and mounted on glass slides to examine potential changes in interlayer spacing following YM155 loading. Fourier transform infrared spectroscopy (FTIR) was carried out by mixing lyophilized samples with potassium bromide and pressing the mixture into pellets for transmittance analysis. Dried LDH-YM155 specimens fixed on conductive tape were examined by X-ray photoelectron spectroscopy (XPS) for the analysis of their surface elemental states.

To evaluate dispersion stability under physiologically relevant conditions, LDH-YM155 was dispersed in H_2O, PBS, or serum-containing DMEM. Zeta potential and PDI were measured after incubation to assess colloidal stability.

To observe acid-responsive structural changes, LDH-YM155 was incubated under acidic conditions at pH 5.5 for different time periods. Samples were collected, deposited onto copper grids, and observed by transmission electron microscopy. LDH-YM155 incubated at pH 7.4 was used as a physiological pH comparison.

For *in vitro* release analysis, LDH-YM155 was dispersed in release media at pH 7.4 or pH 5.5 and incubated at 37 °C. At

predetermined time points, samples were centrifuged, and the released YM155 in the supernatant was collected. The released YM155 solution was alkalized with 0.1 M NaOH before absorbance detection at 450 nm, and the YM155 concentration was determined using the corresponding standard curve. Fresh release medium was added after each sampling. The release profile was plotted as YM155 concentration over time.

2.3 Cellular uptake assay

LDH was labeled with Cy5 to evaluate cellular uptake. Hepa1-6 cells were incubated with Cy5-labeled LDH for different time periods, followed by washing with PBS to remove extracellular particles. Cellular uptake was analyzed by confocal microscopy and flow cytometry.

For uptake inhibition studies, cells were incubated at 4 °C or pretreated with Pitstop 2 (20 μM) before exposure to Cy5-labeled LDH. Cy5 fluorescence intensity was measured by flow cytometry to evaluate the effect of uptake inhibition.

2.4 Cytotoxicity assay

Cell viability following nanoparticle exposure was examined using a CCK-8 assay. Hepa1-6 or SK-Hep1 cells were plated in 96 well plates at 8×10^3 cells per well and maintained to allow stable attachment. The cells were subsequently exposed to YM155, LDH or LDH-YM155 suspensions at final concentrations of 0, 12, 20, 25, 50, or 100 μg mL^{-1} and incubated for 24 h. At the end of the exposure period, CCK-8 solution (10 μL per well) was introduced directly into the culture medium, and the plates were incubated for an additional 30 min at 37 °C. Absorbance was recorded at 450 nm using a microplate reader, and cell viability was expressed as a percentage relative to untreated control cells.

For inhibitor rescue experiments, Hepa1-6 cells were pretreated with Z-VAD-FMK (20 μM), MCC950 (10 μM), Nec-1 (30 μM), NAC (5 mM), Ferrostatin-1 (1 μM), or TTM (50 μM) for 3 h before LDH-YM155 treatment. Cell viability was then measured using the CCK-8 assay.

2.5 Intracellular ROS detection

To measure whether LDH and LDH-YM155 triggered oxidative stress in cells, we detect ROS levels by DCFH-DA probe. Hepa1-6 cells were first treated with 10 μg mL^{-1} of either material for 24 hours. After that, the cells were loaded with DCFH-DA (10 μM) and left to incubate at 37 °C for 30 min. Once the unbound probe was washed away with PBS, fluorescence signals were observed using an inverted fluorescence microscope (excitation at 488 nm) to check for any green signals. For a more quantitative readout, the samples were also run through flow cytometry.

Mitochondrial ROS generation was detected using MitoSOX staining. After treatment, Hepa1-6 cells were incubated with MitoSOX Red working solution (5 μM) under light-protected conditions, washed with PBS, and analyzed by fluorescence microscopy or flow cytometry.

2.6 Mitochondrial membrane potential ($\Delta\Psi m$) analysis by JC-1 staining

Changes in mitochondrial membrane potential were assessed with the JC-1 dye. After exposing Hepa1-6 cells to 10 μg mL^{-1} of LDH or LDH-YM155 for 24 hours, we swapped the culture medium for JC-1 working solution and incubated the cells for another 30 minutes at 37 °C. Once the extra dye was rinsed off with PBS, the cells were taken straight to the flow cytometer. A drop in membrane potential shows up as a shift, instead of forming red aggregates in healthy mitochondria, the JC-1 stays as green monomers.

2.7 Apoptosis analysis

To figure out whether the treatments were pushing cells into apoptosis, we used the Annexin V-FITC/PI dual staining method. Cells were treated with 10 μg mL^{-1} of LDH, LDH-YM155, and equivalent concentration YM155 for 24 hours, then harvested and washed twice. After resuspending them in binding buffer, we added Annexin V-FITC and PI one after the other and let the mixture sit for 15 minutes, keeping it away from light. Finally, the stained cells were analyzed by flow cytometry, which let us tell apart the live ones from the early apoptotic and late apoptotic populations.

2.8 Live-cell Caspase-3 activity detection (GreenNuc™ assay)

Caspase-3 activity in live Hepa1-6 cells was evaluated by GreenNuc™ Live Cell Caspase-3 Activity Assay Kit according to the manufacturer's protocol. Hepa1-6 cells were seeded in 6-well plates or confocal dishes and allowed to adhere overnight. Cells were then treated with LDH or LDH-YM155 (10 μg mL^{-1}) for 24 h. After treatment, GreenNuc™ working solution was added directly to the culture medium and incubated at 37 °C for 30 min under light-protected conditions.

For flow cytometry analysis, cells were collected in PBS for immediate detection. For confocal imaging, treated cells cultured in confocal dishes were observed using a confocal microscope. Green fluorescence signals were recorded to visualize intracellular caspase-3 activation in live cells.

2.9 Caspase-1 and Caspase-8 activity assays

Caspase-1 and caspase-8 activities in Hepa1-6 cells were measured using colorimetric activity assay kits according to the manufacturers' protocols. Briefly, Hepa1-6 cells were seeded in 6-well plates and allowed to adhere overnight. Cells were then treated with LDH or LDH-YM155 (10 μg mL^{-1}) for 24 h. After treatment, cells were harvested, washed with cold PBS, and lysed with the provided lysis buffer on ice.

The cell lysates were centrifuged to remove insoluble debris, and the supernatants were collected for activity measurement. Equal amounts of protein from each sample were incubated with the corresponding caspase-specific pNA-conjugated substrate at 37 °C for the recommended reaction time. Upon cleavage by active caspase-1 or caspase-8, free p-nitroanilide (pNA) was released and detected by measuring absorbance at 405 nm using a microplate reader.

Caspase-1 and caspase-8 activities were calculated according to the absorbance values at 405 nm.

2.10 Lactate dehydrogenase release assay

To assess whether cell membrane integrity was compromised after treatment, we measured LDH release into the culture medium. Hepa1-6 cells were plated with 10 μg mL^{-1} of LDH or LDH-YM155 for 24 hours. Culture supernatants were collected and spun down at 3000 rpm for 5 minutes to get rid of any floating cells or debris. The clear supernatant was then mixed with the LDH reaction reagent and left to incubate for 30 min. Absorbance at 490 nm was detected. To calculate LDH release, we normalized the values to the maximum release control—samples treated with cell lysis buffer to kill all cells.

2.11 Immunofluorescence staining of cultured cells

We next used immunofluorescence staining to observe the changes in the expression or intracellular distribution of markers linked to PANoptosis. Hepa1-6 cells were seeded and treated with 10 μg mL^{-1} of LDH or LDH-YM155 for 24 hours. Then, the cells were fixed with 4% paraformaldehyde for 15 minutes. For staining of intracellular targets, we permeabilized the cells with 0.1% Triton X-100 for 10 minutes. Primary antibodies were applied and left to incubate overnight at 4 °C. The next day, after washing off unbound primary antibodies, we added secondary antibodies and incubated for another hour. DAPI was used to stain the nuclei. Images were captured on a confocal microscope. Where needed, we quantified signal intensity or checked subcellular localization using ImageJ.

2.12 Flow cytometry and imaging flow cytometry analysis

To examine protein expression at the single-cell level, we harvested Hepa1-6 cells after 24 hours of treatment with 10 μg mL^{-1} LDH or LDH-YM155. The cells were pelleted and rinsed twice with ice-cold PBS before antibody staining. For surface markers, we skipped the permeabilization step-cells were simply resuspended in staining buffer containing the primary antibodies and left to incubate at 4 °C for 30 minutes. For intracellular targets, the cells were fixed and permeabilized to allow antibodies to get in. After primary incubation, fluorophore-conjugated secondary antibodies were added for another 30 minutes at 4 °C. Stained samples were then run on a flow cytometer or an imaging flow cytometer, and median fluorescence intensity was recorded for each condition.

2.13 Dendritic cell maturation assay

To evaluate whether the treatment changed how tumor cells talk to immune cells, we collected supernatants from Hepa1-6 cells treated with 10 μg mL^{-1} LDH or LDH-YM155 for 24 hours. These supernatants were spun down at 3000 rpm for 10 minutes to clear out any debris, then transferred onto cultured DC 2.4 cells. After 24 hours of incubation, the dendritic cells were harvested and stained for the maturation markers CD80 and CD86. Flow cytometry was used to evaluate the proportion of maturated DC.

2.14 Transcriptome sequencing and bioinformatic analysis

Transcriptome sequencing was performed to evaluate the global transcriptional response of Hepa1-6 cells after LDH-YM155 treatment. Three independent biological replicates were included for each group. Total RNA was extracted from PBS- or LDH-YM155-treated cells using TRIzol reagent according to the manufacturer's instructions. RNA quality and concentration were assessed using a NanoDrop spectrophotometer and an Agilent 2100 Bioanalyzer. Qualified RNA samples were used for library construction and sequencing on an Illumina platform.

Raw reads were quality-controlled using Fastp and aligned to the reference genome using HISAT2. Gene expression levels were quantified using RSEM. Differentially expressed genes were identified using DESeq2/DEGseq. Multiple testing correction was applied using the false discovery rate (FDR), and genes with $|\log2FC| \geq 1$ and FDR < 0.05 were considered significantly differentially expressed. GO, KEGG, and GSEA analyses were performed to evaluate enriched biological functions and pathways. Transcriptome sequencing and primary bioinformatic analysis were performed by Majorbio Bio-Pharm Technology Co., Ltd. (Shanghai, China).

2.15 *In vivo* antitumor efficacy evaluation

A subcutaneous hepatocellular carcinoma model was established using male C57BL/6 mice aged 6 to 8 weeks. Hepa1-6 cells in the exponential growth phase (1×10^6 cells in 100 μL PBS) were injected subcutaneously into the right flank. Tumors were allowed to develop for 5 days until the mean tumor volume reached around 50 mm^3.Then, randomly allocated mice into treatment groups and intravenous injected PBS, LDH, or LDH-YM155 at a dose of 2 mg kg^{-1} every other day, for a total of seven administrations. Tumor dimensions and body weight were recorded at two day intervals. Tumor volume was estimated using the formula (length × $width^2$)/2, and animal condition was monitored throughout the study. All animal experiments were performed in accordance with the guidelines approved by the Animal Ethics Committee of Chongqing University and complied with relevant institutional and national regulations for the care and use of laboratory animals.

2.16 *In vivo* fluorescence imaging

To visualize *in vivo* distribution, LDH nanoparticles were labeled with indocyanine green (ICG). Tumor-bearing mice received intravenous injections of either free ICG or ICG labeled LDH at an equivalent ICG dose. Whole body fluorescence images were collected at different timepoint post injection using an *in vivo* imaging system (excitation: 745 nm; emission: 810 nm). At 12 h after administration, harvested tumors together with major organs were excised for fluorescence imaging to examine nanoparticle distribution.

2.17 H&E staining of tumor tissues

To examine tumor histopathology, we collected tumor tissues from mice, fixed and embedded. Sections cut at 4 μm were

deparaffinized, rehydrated, and stained with hematoxylin (5 min) followed by eosin (2 min). After dehydration through an ethanol series and clearing with xylene, the slides were mounted with neutral resin and visualized under a light microscope.

2.18 TUNEL assay for apoptosis detection

To locate the apoptosis cells, we used a fluorescence-based TUNEL assay for labels fragmented DNA with a green signal. Sections (4 μm) were deparaffinized, rehydrated, and then treated with proteinase K for 20 minutes at room temperature to help the reagents get in. After that, the TUNEL reaction mix was applied, and the sections were left to incubate at 37 °C for 1 hour in a humidified chamber to keep them from drying out. Once the staining was done, we washed off unbound reagents and counterstained the nuclei with DAPI. TUNEL-positive cells showed up green under 488 nm excitation on a fluorescence microscope.

2.19 Immunofluorescence staining of tumor tissue sections

We also used immunofluorescence to observe the certain proteins were expressed or localized in the tumor tissues. Tumor samples were fixed in 4% paraformaldehyde at 4 °C, paraffin-embedded, and sliced into 4 μm sections. Before staining, the sections went through deparaffinization and rehydration, followed by antigen retrieval—basically heating them in citrate buffer at 95 °C for 20 minutes for unmask epitopes. Then, we blocked non-specific binding with 5% bovine serum albumin for 1 hour. Primary antibodies were added and left to incubate overnight at 4 °C. After washing off the unbound primary antibodies, we added secondary antibodies and incubated for another hour, keeping the slides in the dark. Stain the nuclei with DAPI. Images were captured on a confocal microscope.

2.20 Hemolysis assay

The hemocompatibility of LDH and LDH-YM155 was evaluated using a red blood cell hemolysis assay. Fresh mouse blood was collected in EDTA coated tubes and diluted with PBS. Red blood cells were isolated and resuspended to a final concentration of 2% (v/v). The RBC suspension was incubated with LDH or LDH-YM155 at concentrations ranging from 20 to 400 μg mL^{-1} at 37 °C for 4 h. PBS and double distilled water served as negative and positive controls, respectively. Following incubation, samples were centrifuged at 3000 rpm for 15 min. Hemolysis was assessed visually, and hemoglobin release was quantified by measuring absorbance at 541 nm when required.

2.21 Routine blood analysis

At the endpoint of the animal experiment, blood samples were collected from mice into anticoagulant tubes. Routine blood parameters, including white blood cell count, red blood cell count, lymphocyte-related indices, granulocyte-related indices, monocyte count, hematocrit, and mean platelet volume, were measured using an automated hematology analyzer.

2.22 Statistical analysis

Data are presented as mean ± SD. Statistical analysis was performed using GraphPad Prism. Comparisons among multiple groups were analyzed by one-way ANOVA followed by multiple comparisons test. Tumor growth curves were analyzed by two-way ANOVA. A value of $P < 0.05$ was considered statistically significant.

3 Results and discussion

3.1 Preparation and Characterization of LDH and LDH-YM155

To develop an effective delivery platform for the pro-apoptotic agent YM155, magnesium–aluminum layered double hydroxide nanosheets were synthesized *via* a co-precipitation method and subsequently loaded with YM155 through electrostatic interaction and interlayer incorporation. The nanocomposites obtained after YM155 loading, referred to as LDH-YM155, were characterized to examine their morphological, structural, and surface-related features.

Scanning electron microscopy (SEM) images showed that pristine LDH nanosheets exhibited a plate-like morphology (Fig. 2A). A comparable morphology was observed for LDH-YM155 (Fig. 2B), suggesting that the overall nanosheet architecture was preserved following drug loading. Atomic force microscopy (AFM) analysis further revealed sheet-like structures for LDH-YM155, with the thickness of individual nanosheets ranging from approximately 11 to 16 nm across three representative measurement lines (Fig. 2C).

The crystalline features of the materials were examined by X-ray diffraction (XRD) (Fig. 2D). Pristine LDH displayed diffraction peaks characteristic of the MgAl-layered double hydroxide phase (PDF#35-0965), confirming the formation of a layered structure. After YM155 loading, LDH–YM155 retained the typical (003), (006), and (012) reflections associated with LDH. Minor variations in peak intensity and position were observed, indicating that the layered framework remained largely intact while undergoing subtle structural changes upon drug incorporation.

FTIR spectroscopy was used to probe chemical features of the nanocomposites (Fig. 2E). The spectrum of YM155 exhibited characteristic vibrational bands corresponding to its functional groups. In the LDH-YM155 spectrum, several of these bands were detectable alongside the intrinsic LDH signals, together with additional absorption features not present in pristine LDH, suggesting the association of YM155 with the LDH matrix.

XPS analysis was performed to further assess the elemental composition of LDH-YM155 (Fig. 2F). The survey spectrum showed the presence of Mg, Al, and O, consistent with the MgAl-LDH framework. In addition, pronounced C signals and a detectable N peak were observed in the LDH-YM155 sample. As nitrogen is absent in pristine LDH, the appearance of the N signal supports the incorporation of YM155 within the nanocomposite.

To further characterize the drug-loading performance of the LDH nanocarrier, the drug loading capacity and encapsulation

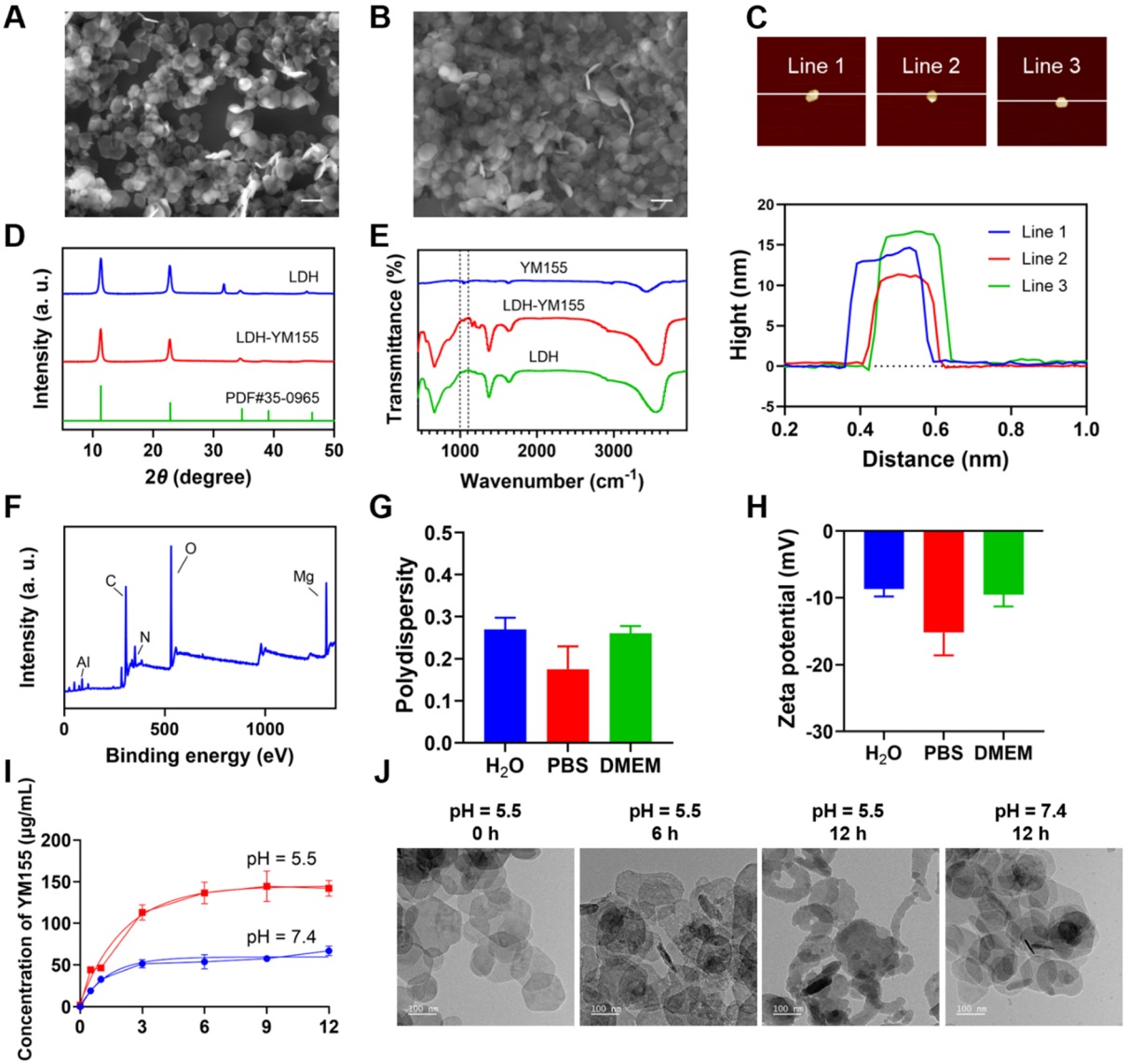

Fig. 2 Preparation and Characterization of LDH and LDH-YM155. (A and B) The representative SEM image of LDH (A) and LDH-YM155 (B). Scale bar: 200 nm. (C) AFM images and the thickness analysis of LDH-YM155 in three different views. (D) XRD patterns of LDH, LDH-YM155, and the standard MgAl-LDH (PDF#35-0965, $Mg_6Al_2(OH)18{\cdot}4.5H_2O$). (E) FTIR spectra of YM155, LDH, and LDH-YM155. (F) XPS analysis of LDH-YM155. (G and H) PDI and zeta potential of LDH-YM155 dispersed in H_2O, PBS, and serum-containing DMEM. (I) *In vitro* release profiles of YM155 from LDH-YM155 under physiological and acidic conditions at pH 7.4 and pH 5.5. (J) TEM images of LDH-YM155 after incubation under acidic conditions at pH 5.5 for 0, 6, and 12 h, and under physiological pH 7.4 for 12 h. Data are presented as mean ± SD, $n = 3$.

efficiency of YM155 in LDH-YM155 were quantified. LDH-YM155 achieved a drug loading capacity of 21.25% and an encapsulation efficiency of 27%, confirming effective incorporation of YM155 into the LDH nanosheet system.

The colloidal stability of LDH-YM155 was subsequently assessed under aqueous and physiologically relevant conditions. After dispersion in H_2O, PBS, or serum-containing DMEM, LDH-YM155 showed no significant changes in PDI or zeta potential, indicating that the nanocomposite maintained stable dispersion properties in both physiological buffer and serum-containing medium (Fig. 2G and H).

The pH-responsive release behavior of LDH-YM155 was further evaluated under physiological and acidic conditions. YM155 release was markedly enhanced at pH 5.5 compared with pH 7.4. Within 12 h, the released YM155 concentration reached 142.09 μg mL^{-1} at pH 5.5, whereas only 66.97 μg mL^{-1} was detected at pH 7.4, demonstrating acid-facilitated YM155 release from the LDH carrier (Fig. 2I). Consistent with this release profile, TEM imaging showed progressive disassembly of LDH-YM155 nanosheets under acidic conditions, while the nanosheet architecture was relatively preserved after 12 h at pH 7.4 (Fig. 2J). These findings indicate that LDH-YM155 undergoes acid-responsive structural degradation, thereby facilitating YM155 release under acidic microenvironmental conditions.

Collectively, these results demonstrate the successful preparation of LDH-YM155, characterized by efficient YM155

loading, preserved nanosheet architecture, stable dispersion under physiological and serum-containing conditions, and acid-responsive drug release behavior.

3.2 LDH-YM155 is efficiently internalized and induces early cellular stress in Hepa1-6 cells

After confirming the successful construction and physicochemical stability of the LDH-YM155 nanocomposite, its cellular uptake behavior and stress-related biological effects were further evaluated in hepatocellular carcinoma Hepa1-6 cells. Efficient intracellular delivery is a prerequisite for YM155 to exert its pharmacological function, and thus the internalization of LDH-YM155 was first examined. To evaluate whether LDH-YM155 could be efficiently internalized by hepatocellular carcinoma cells, Cy5-labeled LDH was incubated with Hepa1-6 cells to monitor cellular uptake. Microscopy and flow cytometry analysis revealed minimal Cy5 fluorescence at 0 h and a clear increase in intracellular Cy5 signal after incubation, confirming progressive intracellular accumulation of Cy5-LDH in Hepa1-6 cells (Fig. 3A and B). Quantitative analysis of median fluorescence intensity (MFI) demonstrated a significant increase in Cy5 signal at 1 h and 3 h compared with 0 h, supporting efficient cellular internalization of LDH-YM155 in a time-dependent manner (Fig. 3C).

The cellular uptake mechanism was further examined by exposing Hepa1-6 cells to Cy5-LDH under uptake-inhibitory

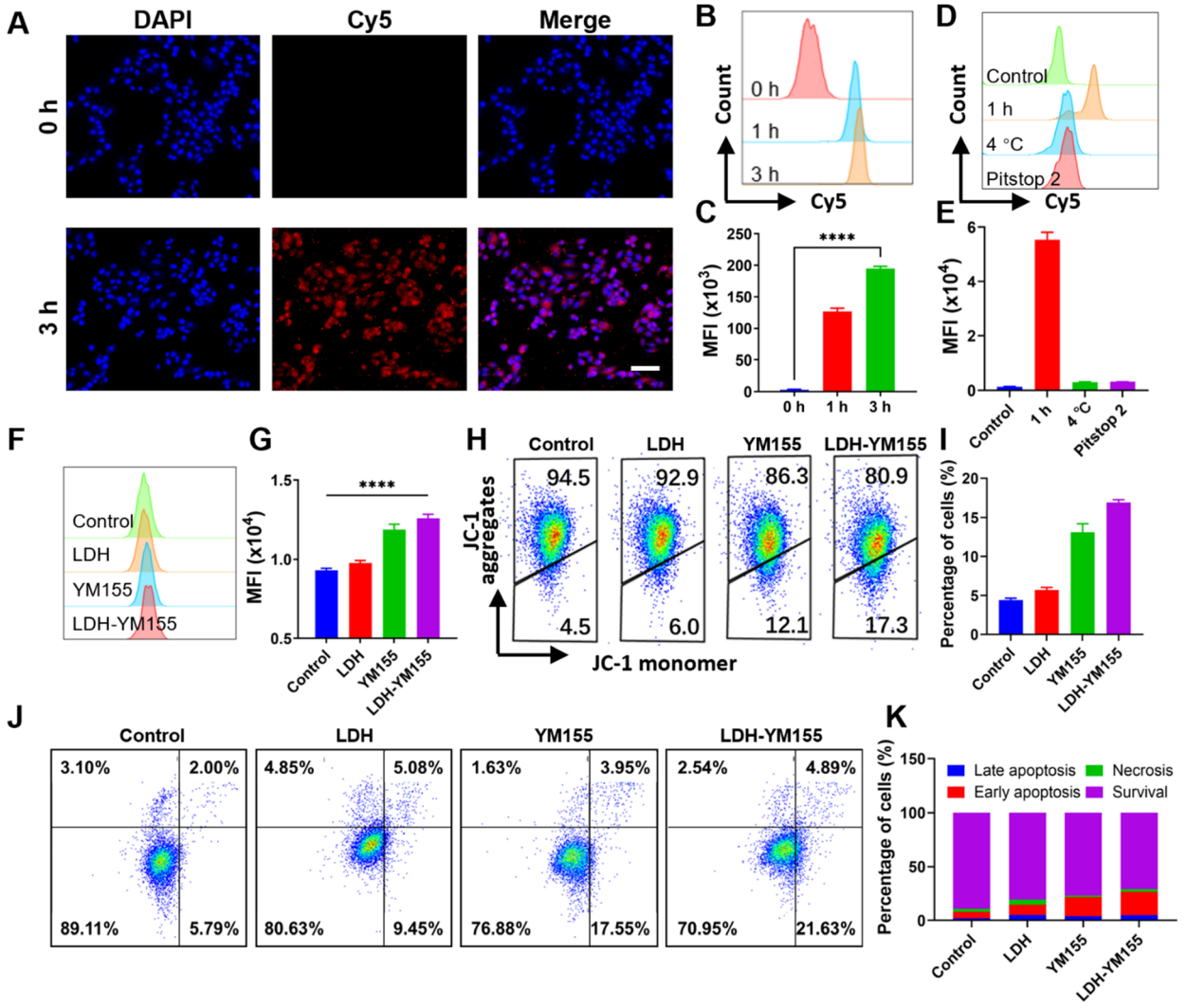

Fig. 3 Cellular uptake and intracellular stress responses induced by LDH-YM155 in Hepa1-6 cells. (A) Confocal images of Cy5-labeled LDH uptake in Hepa1-6 cells at 0 h and 3 h. Nuclei were stained with DAPI. Scale bar: 100 μm. (B) Flow cytometry histograms of Cy5 fluorescence intensity after incubation with Cy5-LDH. (C) Quantification of Cy5 MFI at different incubation times. (D) Representative flow cytometry histograms showing Cy5-LDH uptake after incubation at 4 °C or pretreatment with Pitstop 2. (E) Quantification of Cy5 fluorescence MFI under uptake-inhibition conditions. (F) Representative flow cytometry histograms of intracellular ROS levels after different treatments. (G) Quantification of ROS fluorescence MFI. (H) Representative JC-1 flow cytometry plots showing mitochondrial membrane potential changes. (I) Quantification of JC-1 monomer-positive cells. (J) Representative Annexin V-FITC/PI flow cytometry plots. (K) Quantification of viable, early apoptotic, late apoptotic, and necrotic cells. Data are presented as mean ± SD, $n = 3$. ****$P < 0.0001$. Statistical significance was determined by one-way ANOVA followed by Tukey's multiple comparisons test. Scale bar: 100 μm.

conditions. Incubation at 4 °C markedly reduced Cy5-LDH internalization, indicating that LDH uptake is primarily mediated by an energy-dependent active process rather than passive membrane association. Pretreatment with Pitstop 2, a clathrin-mediated endocytosis inhibitor, also significantly decreased intracellular Cy5 fluorescence. These results suggest that LDH internalization in Hepa1-6 cells occurs predominantly through energy-dependent endocytosis, with clathrin-mediated endocytosis contributing substantially to the uptake process (Fig. 3D and E).

After confirming cellular uptake, we next investigated whether LDH-YM155 induced oxidative stress in Hepa1-6 cells. ROS generation was assessed using the DCFH-DA probe. Flow cytometry analysis showed that LDH alone caused only minimal ROS elevation compared with the control group, whereas YM155 and LDH-YM155 increased intracellular ROS-associated fluorescence intensity, with LDH-YM155 producing the strongest response (Fig. 3F). Quantitative MFI analysis showed that ROS levels were significantly higher in the LDH-YM155 group than in the control and LDH groups (Fig. 3G).

Given that excessive ROS generation is closely associated with mitochondrial injury, $\Delta\Psi$m was further examined using JC-1 staining. Flow cytometry results showed that LDH-YM155 treatment induced a pronounced shift toward reduced mitochondrial membrane potential compared with the control and LDH groups (Fig. 3H). Quantitative analysis further demonstrated that the percentage of cells with decreased $\Delta\Psi$m was significantly increased after LDH-YM155 treatment, indicating mitochondrial depolarization (Fig. 3I).

Early cell-death responses were examined using Annexin V-FITC/PI staining. LDH alone induced only minor changes relative to the control group, whereas free YM155 increased the apoptotic cell population. Under equivalent YM155 treatment conditions, LDH-YM155 produced a greater reduction in viable cells and a more pronounced increase in apoptotic fractions than free YM155, indicating that LDH-mediated delivery enhanced YM155-induced tumor cell death (Fig. 3J and K).

Together, these findings demonstrate that LDH-YM155 is rapidly internalized by Hepa1-6 cells through an energy-dependent endocytic process involving clathrin-mediated endocytosis and triggers pronounced oxidative stress accompanied by mitochondrial membrane potential disruption and apoptotic cell-death progression. This intracellular stress response provides a mechanistic basis for subsequent activation of regulated cell death pathways induced by LDH-YM155.

3.3 LDH-YM155 suppresses Survivin and induces mitochondrial oxidative stress in HCC cells

LDH-YM155 was first evaluated for antitumor activity in both murine and human HCC cell models using CCK-8 assays. In Hepa1-6 cells, bare LDH showed minimal cytotoxicity across the tested concentration range, whereas LDH-YM155 markedly reduced cell viability in a dose-dependent manner (Fig. 4A). This inhibitory effect was also observed in the human HCC cell line SK-Hep1, in which LDH-YM155 produced a clear reduction in cell viability compared with LDH alone (Fig. 4B). These results indicate that LDH-YM155 exhibits cytotoxic activity in both Hepa1-6 and SK-Hep1 HCC cells.

Given that YM155 targets Survivin, we then examined whether LDH-mediated delivery preserved its Survivin-suppressive activity (Fig. 4C). Flow cytometry revealed a progressive decrease in Survivin fluorescence following LDH-YM155 treatment, with reduced expression evident at 12 h and further suppression observed at 24 h (Fig. 4D and E). A dose-dependent pattern was also observed, as increasing LDH-YM155 concentrations induced a leftward shift in Survivin fluorescence and a corresponding reduction in MFI values (Fig. 4F and G). These findings demonstrate that YM155 retains its ability to suppress Survivin expression after incorporation into the LDH nanocarrier.

Survivin suppression was accompanied by pronounced mitochondrial oxidative stress. MitoSOX fluorescence imaging showed stronger mitochondrial ROS signals in LDH-YM155-treated cells than in the control and LDH groups (Fig. 4H). Consistently, flow cytometry confirmed elevated mitochondrial ROS fluorescence after LDH-YM155 treatment (Fig. 4I and J), indicating substantial mitochondrial ROS accumulation in Hepa1-6 cells.

Cytochrome *c* distribution was further examined to determine whether mitochondrial oxidative stress was associated with mitochondrial injury. In control and LDH-treated cells, Cytochrome *c* remained predominantly localized to mitochondria. By contrast, LDH-YM155 treatment resulted in a more diffuse cytoplasmic Cytochrome *c* pattern, indicating release from mitochondria (Fig. 4K). This redistribution links LDH-YM155-induced mitochondrial stress to the activation of mitochondria-associated cell-death signaling.

Together, these results show that LDH-YM155 reduces viability in both murine and human HCC cells, suppresses Survivin expression in a time- and dose-dependent manner, and induces mitochondrial ROS accumulation accompanied by Cytochrome *c* release.

3.4 LDH-YM155 induces PANoptosis in Hepa1-6 cells

Following the uptake-driven oxidative and mitochondrial stress responses, we next characterized the downstream cell death phenotype induced by LDH-YM155. To delineate the contribution of distinct regulated cell death programs to LDH-YM155-induced cytotoxicity, Hepa1-6 cells were pretreated with pathway-selective inhibitors prior to LDH-YM155 exposure. Relative to LDH-YM155 treatment alone, pharmacological inhibition with Z-VAD-FMK, MCC950, Nec-1, or NAC partially rescued cell viability, implicating caspase-dependent apoptotic signaling, NLRP3 inflammasome-associated activation, necroptotic signaling, and oxidative stress in the observed cytotoxic response. By contrast, Ferrostatin-1 and TTM failed to confer comparable protection, suggesting that ferroptosis- and cuproptosis-dominant mechanisms were not the principal drivers of LDH-YM155-mediated cell death under these experimental conditions (Fig. 5A).

Because PANoptosis is defined by coordinated engagement of apoptotic execution and inflammatory cell death signaling,

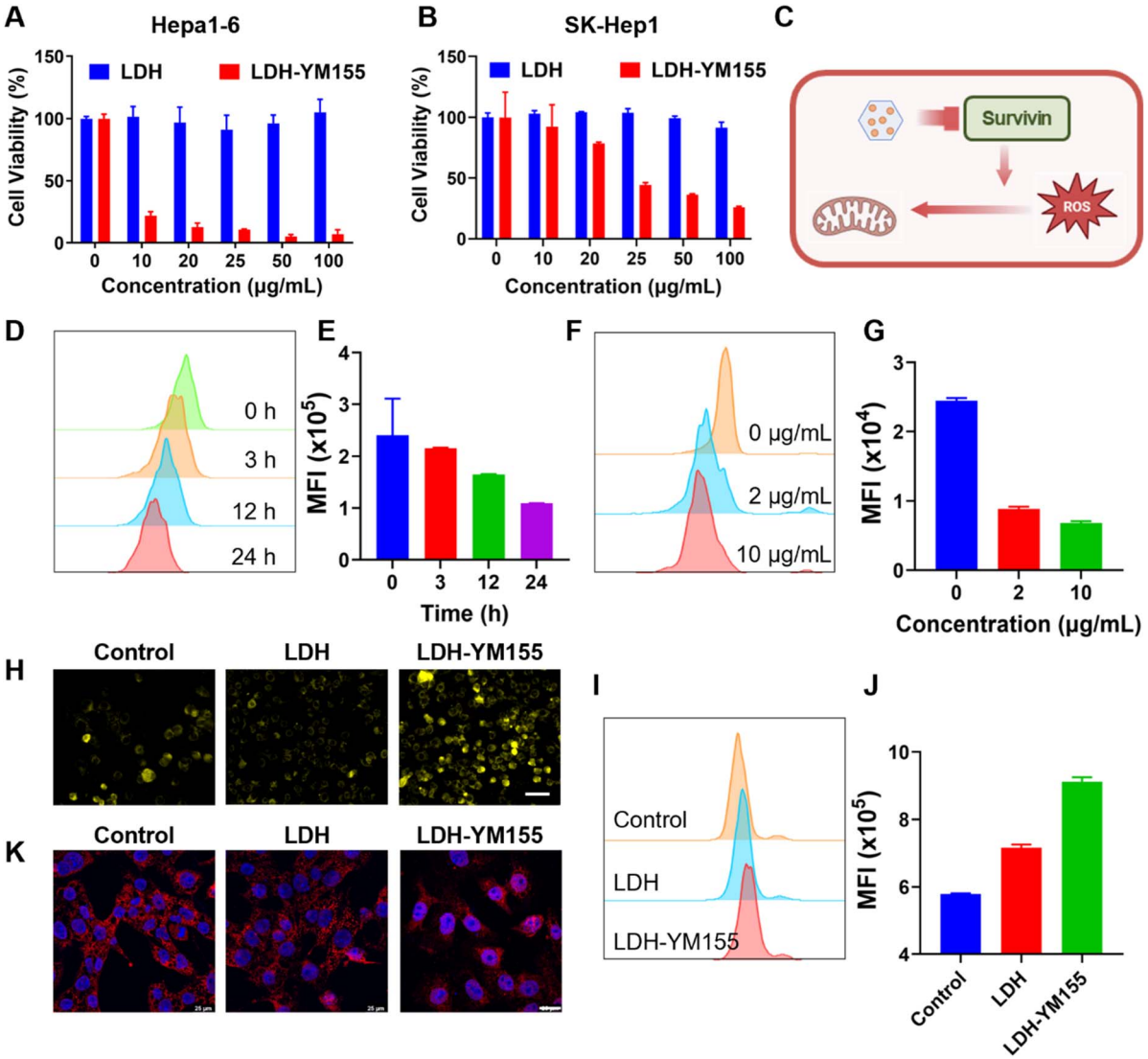

Fig. 4 LDH-YM155 suppresses Survivin and induces mitochondrial oxidative stress in HCC cells. (A) Cell viability of Hepa1-6 cells after treatment with different concentrations of LDH or LDH-YM155. (B) Cell viability of SK-Hep1 cells after treatment with different concentrations of LDH or LDH-YM155. (C) Schematic illustration showing LDH-YM155-mediated Survivin suppression and mitochondrial ROS induction. (D) Representative flow cytometry histograms showing time-dependent Survivin expression after LDH-YM155 treatment. (E) Quantification of Survivin fluorescence MFI at different treatment times. (F) Representative flow cytometry histograms showing dose-dependent Survivin expression after LDH-YM155 treatment. (G) Quantification of Survivin fluorescence MFI at different LDH-YM155 concentrations. (H) Representative MitoSOX fluorescence images showing mitochondrial ROS generation after different treatments. Scale bar: 100 μm. (I) Representative flow cytometry histograms of mitochondrial ROS levels. (J) Quantification of mitochondrial ROS fluorescence MFI. (K) Representative immunofluorescence images showing Cytochrome *c* release after different treatments. Scale bar: 25 μm. Data are presented as mean ± SD, $n = 3$. Statistical significance was determined by one-way ANOVA followed by multiple comparisons test.

we next examined markers associated with these branches. Caspase-3 activation was assessed using the GreenNuc live-cell probe. As a key executioner protease, caspase-3 activation represents a hallmark event of apoptosis-associated cell death progression. Compared with control and LDH, LDH-YM155 treatment produced stronger GreenNuc signals in the merged images, indicating increased caspase-3 activity (Fig. 5B). In addition, caspase-8 activity was increased after LDH-YM155 treatment, suggesting activation of an upstream caspase node involved in apoptosis and PANoptosis-related inflammatory cell death regulation (Fig. 5C).

In parallel, inflammasome-associated signaling was evaluated by NLRP3, which functions as a central inflammasome sensor and plays an essential role in initiating pyroptosis-related inflammatory signaling. Flow cytometry revealed a pronounced increase in NLRP3 fluorescence intensity in the LDH-YM155 group relative to the control and LDH groups, and MFI quantification further confirmed significant upregulation of NLRP3 expression (Fig. 5D and E). This increase was corroborated by immunofluorescence staining, which showed stronger intracellular NLRP3 signals after LDH-YM155 treatment (Fig. 5F).

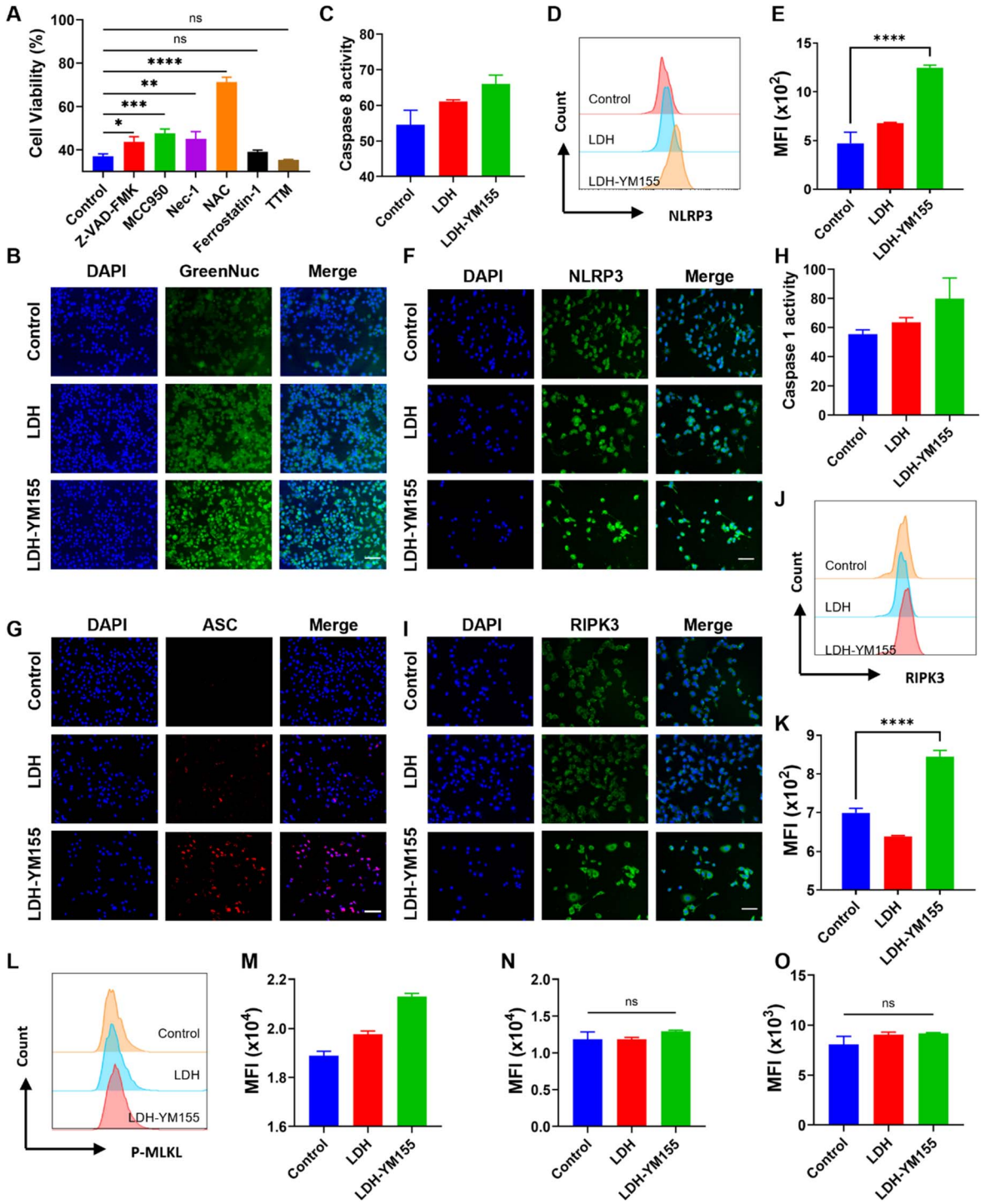

Fig. 5 LDH-YM155 induces PANoptosis in Hepa1-6 cells. (A) Cell viability of Hepa1-6 cells after LDH-YM155 treatment with or without pretreatment using different pathway-related inhibitors. (B) Representative GreenNuc fluorescence images showing caspase-3 activity after different treatments. (C) Quantification of caspase-8 activity. (D) Representative flow cytometry histograms of NLRP3 expression. (E) Quantification of NLRP3 fluorescence MFI. (F) Representative immunofluorescence images of NLRP3 expression. (G) Representative confocal fluorescence images showing ASC speck formation. (H) Quantification of caspase-1 activity. (I) Representative immunofluorescence images of RIPK3 expression. (J) Representative flow cytometry histograms of RIPK3 expression. (K) Quantification of RIPK3 fluorescence MFI. (L) Representative flow cytometry histograms of p-MLKL expression. (M) Quantification of p-MLKL fluorescence MFI. (N and O) Quantification of NLRP3 (N) and RIPK3 (O) fluorescence MFI after Z-VAD-FMK pretreatment. Data are presented as mean ± SD, $n = 3$. Statistical significance was determined by one-way ANOVA followed by multiple comparisons test. ns, not significant; *$P < 0.05$, **$P < 0.01$, ***$P < 0.001$, ****$P < 0.0001$. Scale bar: 100 μm.

To determine whether NLRP3 upregulation was accompanied by inflammasome assembly, ASC speck formation was assessed by confocal microscopy. LDH-YM155 treatment markedly increased punctate ASC signals compared with the control and LDH groups, indicating enhanced formation of inflammasome complexes (Fig. 5G). In parallel, caspase-1 activity was significantly elevated in LDH-YM155-treated cells, providing functional evidence for inflammasome activation and supporting the engagement of inflammasome-associated pyroptotic signaling (Fig. 5H).

Necroptosis-associated signaling was assessed by RIPK3. RIPK3 is a critical kinase regulator in necroptosis signaling and is commonly used as a representative marker reflecting necroptotic pathway activation. Immunofluorescence staining indicated increased RIPK3 signals in the LDH-YM155 group compared with control and LDH (Fig. 5I). Flow cytometry further supported this trend, with a shifted RIPK3 fluorescence distribution and significantly higher RIPK3 MFI after LDH-YM155 treatment (Fig. 5J,K). As phosphorylation of MLKL is a terminal execution event in necroptosis, p-MLKL was further assessed by flow cytometry to determine whether RIPK3 activation progressed to downstream necroptotic execution. LDH-YM155 treatment markedly increased p-MLKL fluorescence intensity compared with the control and LDH groups, indicating activation of the RIPK3/MLKL axis and supporting the engagement of necroptotic signaling in LDH-YM155-induced cell death (Fig. 5L, M).

Finally, to determine whether caspase activity contributed to the coordinated induction of inflammatory and necroptotic markers, Hepa1-6 cells were pretreated with the pan-caspase inhibitor Z-VAD-FMK before subsequent treatment. Following Z-VAD-FMK pretreatment, NLRP3 and RIPK3 expression no longer differed significantly among the treatment groups, in contrast to the marked upregulation observed after LDH-YM155 treatment in the absence of caspase inhibition (Fig. 5N, O). These results suggest that caspase activity is involved in coupling LDH-YM155-induced cell death to the activation of NLRP3- and RIPK3-associated signaling.

Collectively, LDH-YM155 engaged multiple PANoptosis-related signaling branches, including caspase-3/8-associated apoptotic signaling, NLRP3/ASC/caspase-1-associated inflammasome activation, and RIPK3/p-MLKL-associated necroptotic signaling. Together with the inhibitor-rescue results and the Z-VAD-FMK-mediated suppression of NLRP3 and RIPK3 activation, these findings demonstrate that LDH-YM155 induces PANoptosis in Hepa1-6 cells.

3.5 LDH-YM155 promotes ICD-associated DAMP signaling and functional dendritic cell activation

We demonstrated that LDH-YM155 triggers PANoptosis-like programmed cell death in Hepa1-6 cells. Such inflammatory and membrane-disruptive cell death phenotypes are often accompanied by the exposure and release of DAMPs, which may convert tumor cell death into an immunogenic process. Therefore, we further investigated whether LDH-YM155 could induce ICD-associated signals and promote antigen-presenting cell activation.

Calreticulin exposure on the membrane is a hallmark ICD signal that facilitates recognition and phagocytic clearance of dying tumor cells. Under non-permeabilizing staining conditions, immunofluorescence staining showed that LDH-YM155 treatment resulted in markedly enhanced CRT-associated fluorescence compared with the control and LDH groups, indicating increased cell-surface CRT exposure in Hepa1-6 cells (Fig. 6A). Representative flow cytometry histograms showed a clear rightward shift of CRT fluorescence after LDH-YM155 treatment, and MFI quantification further confirmed a significant elevation of surface CRT in the LDH-YM155 group (Fig. 6B and C).

To determine whether LDH-YM155-induced tumor cell death could generate functional immune-stimulatory signals, we established a conditioned-medium coculture model to evaluate dendritic cell (DC) maturation. Specifically, the supernatant from treated Hepa1-6 cells was collected and mixed with fresh medium at a 1 : 1 ratio, followed by incubation with DCs prior to flow cytometric analysis (Fig. 6D). Conditioned medium collected from LDH-YM155-treated Hepa1-6 cells significantly increased the proportion of $CD80^{+}CD86^{+}$ mature DCs compared with conditioned medium from the control and LDH groups (Fig. 6E and F). These findings indicate that LDH-YM155-treated tumor cells release immunostimulatory factors capable of promoting dendritic cell maturation.

High mobility group box 1 (HMGB1) is another representative ICD-associated DAMP involved in immune stimulation. Flow cytometry analysis showed a reduction in intracellular HMGB1-associated fluorescence after LDH-YM155 treatment, suggesting that LDH-YM155-induced cell death was accompanied by HMGB1-associated molecular changes consistent with ICD progression (Fig. 6G and H). To directly verify extracellular HMGB1 release, HMGB1 levels in the culture supernatant were further quantified by ELISA. Extracellular HMGB1 was significantly elevated in the LDH-YM155 group compared with the control and LDH groups, confirming active HMGB1 release rather than an inference based solely on reduced intracellular staining (Fig. 6I).

Extracellular ATP, another canonical ICD-associated DAMP, was also measured in the culture supernatant. LDH-YM155 treatment significantly increased ATP release compared with the control and LDH groups, further supporting the induction of ICD-associated DAMP signaling (Fig. 6J).

Since inflammatory programmed cell death is frequently associated with loss of membrane integrity, we further assessed plasma membrane damage by measuring lactate dehydrogenase (LDH) release into the culture supernatant. Lactate dehydrogenase release was increased after LDH treatment and was further elevated in the LDH-YM155 group, indicating enhanced membrane permeability and late-stage cell rupture during cell death progression (Fig. 6K).

Taken together, LDH-YM155 treatment induced multiple ICD-associated hallmarks, including enhanced surface CRT exposure, extracellular HMGB1 and ATP release, and increased

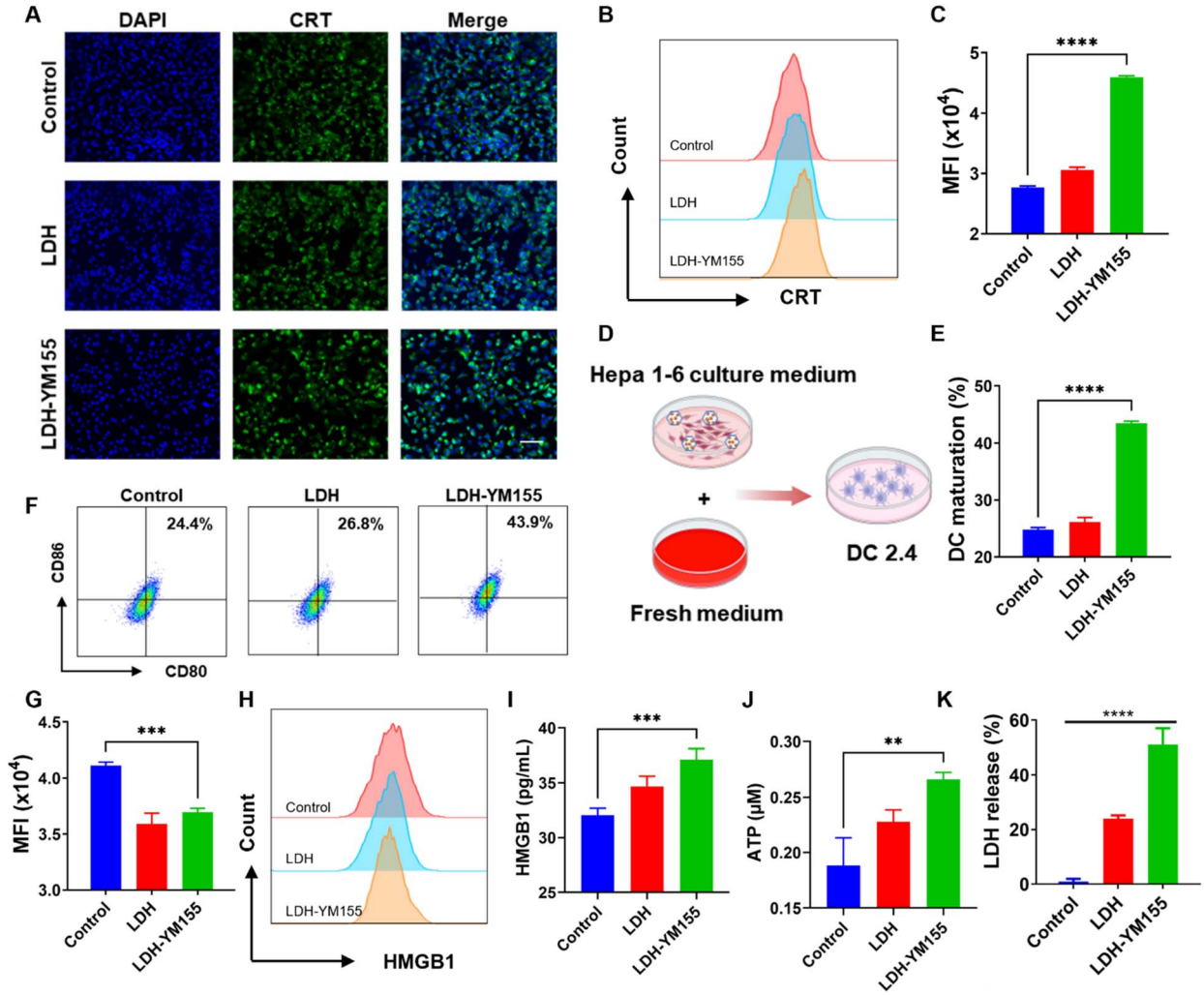

Fig. 6 LDH-YM155 induces ICD and promotes DC maturation. (A) Representative immunofluorescence images showing CRT exposure in Hepa1-6 cells after different treatments under non-permeabilizing staining conditions. (B) Representative flow cytometry histograms of CRT fluorescence. (C) Quantification of CRT fluorescence MFI. (D) Schematic illustration of the conditioned-medium coculture model used to evaluate dendritic cell maturation. (E) Quantification of $CD80^{+}CD86^{+}$ mature DCs after incubation with conditioned medium from differently treated Hepa1-6 cells. (F) Representative flow cytometry plots of CD80 and CD86 expression in DCs. (G) Quantification of intracellular HMGB1 fluorescence MFI in Hepa1-6 cells. (H) Representative flow cytometry histograms of intracellular HMGB1 fluorescence. (I) ELISA quantification of extracellular HMGB1 levels in the culture supernatant. (J) Quantification of extracellular ATP release. (K) Quantification of LDH release. Data are presented as mean ± SD, $n = 3$. Statistical significance was determined by one-way ANOVA followed by multiple comparisons test. $^{**}P < 0.01$, $^{***}P < 0.001$, $^{****}P < 0.0001$. Scale bar: 100 μm.

membrane damage, while simultaneously generating tumor-derived factors capable of promoting dendritic cell maturation.

3.6 Transcriptomic analysis reveals stress and inflammatory signaling programs consistent with PANoptosis

To obtain a global view of the cellular response to LDH-YM155, RNA sequencing was performed comparing LDH-YM155-treated cells with PBS controls. Principal component analysis (PCA) showed a separation between the two groups, indicating that LDH-YM155 induced a distinct transcriptional state rather than a modest shift in baseline expression (Fig. 7A). Differential expression analysis further supported this separation, with 242 upregulated genes and 70 downregulated genes in the LDH-YM155 group relative to PBS (Fig. 7B).

A hub–gene interaction network highlighted rapid stress-response and transcriptional adaptation as a dominant feature of the LDH-YM155 response. Several immediate-early transcription factors and signaling regulators, including Fos, Jun, Fosb, Atf3, Dusp1, and Nr4a1, formed a densely connected module, consistent with a strong stimulus-driven transcriptional program (Fig. 7C).

Functional enrichment analysis indicated that the DEGs were preferentially associated with stimulus and inflammatory-response terms. GO enrichment was dominated by categories such as response to oxygen-containing compound, response to lipid, response to lipopolysaccharide, and broad cellular response to chemical/biotic stimulus, suggesting activation of oxidative stress and innate-like response programs (Fig. 7D).

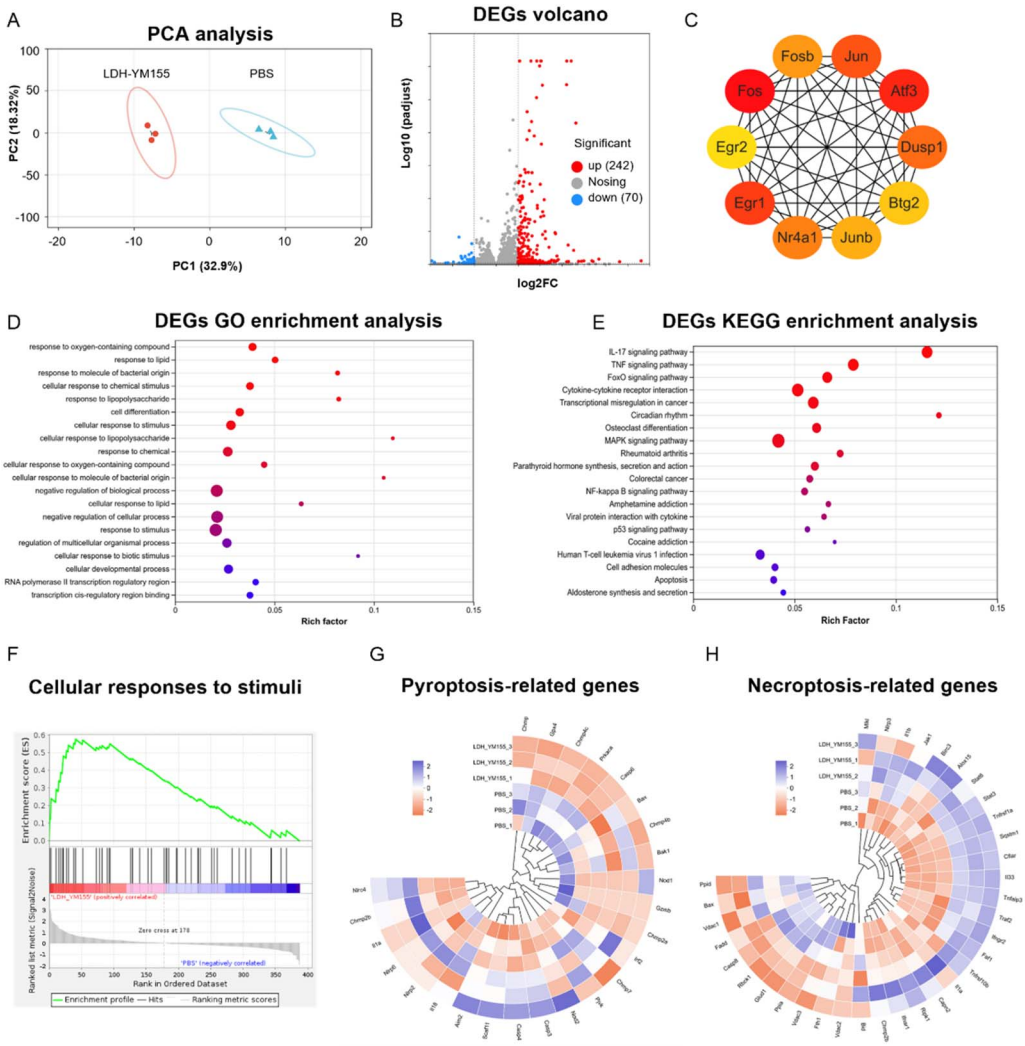

Fig. 7 Transcriptomic profiling of Hepa1-6 cells after LDH-YM155 treatment. (A) PCA plot of LDH-YM155 and PBS treated Hepa 1-6. (B) Volcano plot of DEGs between LDH-YM155 and PBS groups. (C) Protein–protein interaction network of the Top 10 hub genes. (D) GO enrichment analysis of differentially expressed genes. (E) KEGG pathway enrichment analysis of differentially expressed genes. (F) Gene set enrichment analysis (GSEA) plot for REACTOME_CELLULAR_RESPONSES_TO_STIMULI. (G) Heatmap of pyroptosis-related gene expression. (H) Heatmap of necroptosis-related gene expression.

KEGG pathway analysis converged on inflammatory and stress-linked pathways, including IL-17 signaling, TNF signaling, MAPK signaling, cytokine–cytokine receptor interaction, and NF-kappa B signaling, along with apoptosis as an enriched pathway term (Fig. 7E). In line with these enrichment results, gene set enrichment analysis showed that "CELLULAR_RESPONSES_TO_STIMULI" was positively correlated with the LDH-YM155 condition, supporting a global activation of stimulus-response signaling (Fig. 7F).

Because our phenotypic assays indicated PANoptosis rather than a single death modality, we further examined curated gene sets related to pyroptosis and necroptosis. The pyroptosis-related heatmap showed coordinated reprogramming across inflammasome- and gasdermin-associated genes, including Nlrp3 and multiple caspase- and cytokine-linked components (Fig. 7G). The necroptosis-related heatmap likewise demonstrated broad changes across death receptor and downstream signaling-associated genes, including Ripk1 and multiple adaptor/regulatory factors (Fig. 7H). Together, these transcriptomic signatures align with the experimental observation that LDH-YM155 engages stress-responsive programs and inflammatory cell-death-associated pathways, providing molecular-level support for the PANoptosis-like phenotype observed in Hepa1-6 cells.

3.7 *In vivo* antitumor efficacy of LDH-YM155 nanocomposites

To assess the *in vivo* therapeutic performance of LDH-YM155, a subcutaneous Hepa1-6 tumor model was established. When tumors reached around 50 mm^3, mice were randomly divided into 3 groups and treated *via* intravenous injection every other day for a total of seven doses with PBS, LDH, or LDH-YM155.

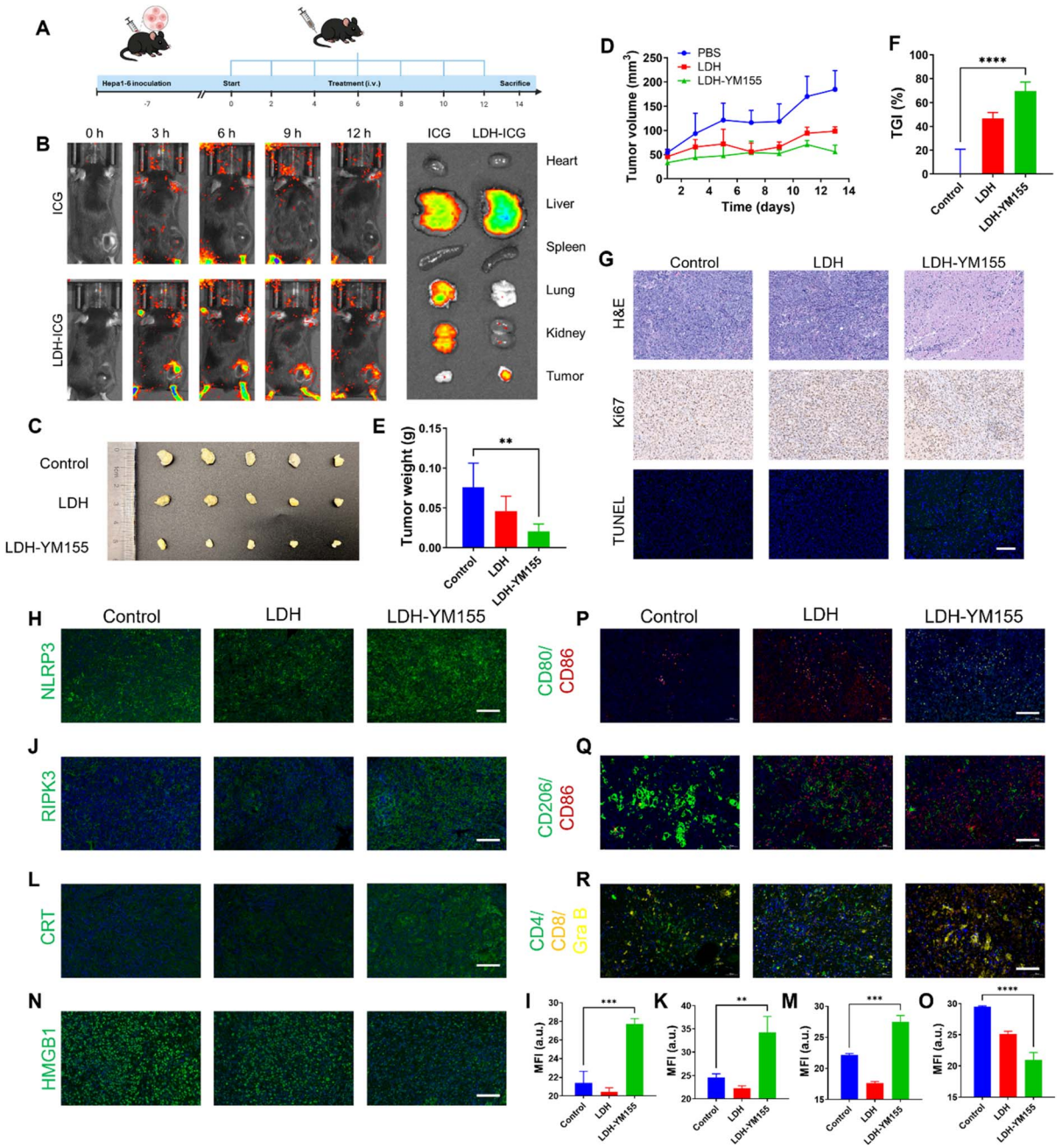

Fig. 8 *In vivo* tumor targeting, antitumor efficacy, and immune microenvironment remodeling induced by LDH-YM155. (A) Schematic illustration of the Hepa1-6 tumor-bearing mouse model, treatment schedule, and endpoint analysis. (B) *In vivo* fluorescence imaging of tumor-bearing mice after injection of free ICG or LDH-ICG at different time points, together with *ex vivo* fluorescence imaging of major organs and tumors. (C) Photographs of excised tumors from different treatment groups. (D) Tumor growth curves during treatment. $n = 5$. (E) Tumor weight at the endpoint. $n = 5$. (F) Tumor growth inhibition rate. $n = 5$. (G) Representative H&E, Ki67, and TUNEL staining images of tumor sections. (H and I) Representative immunofluorescence images and quantitative analysis of NLRP3 expression in tumor tissues. $n = 3$. (J and K) Representative immunofluorescence images and quantitative analysis of RIPK3 expression. $n = 3$. (L and M) Representative immunofluorescence images and quantitative analysis of CRT expression. $n = 3$. (N and O) Representative immunofluorescence images and quantitative analysis of HMGB1 expression. $n = 3$. (P) Representative immunofluorescence images of CD80 and CD86 staining for dendritic cell maturation. (Q) Representative immunofluorescence images of CD86 and CD206 staining for macrophage polarization. (R) Representative immunofluorescence images of CD4, CD8, and Granzyme B staining for T-cell infiltration and cytotoxic activation. Data are presented as mean ± SD. Statistical significance was determined by one-way ANOVA followed by multiple comparisons test. ns, not significant; $^{**}P < 0.01$, $^{***}P < 0.001$, $^{****}P < 0.0001$. Scale bar: 100 μm.

The volumes of tumor were measured throughout the treatment period to monitor tumor progression (Fig. 8A).

To examine the tumor-targeting capability of the nanocarrier system, near-infrared fluorescence imaging was conducted using ICG as a model probe. Free ICG or LDH-loaded ICG (LDH-ICG) was administered *via* tail vein injection. As shown in Fig. 8B, whole-body fluorescence imaging demonstrated that LDH-ICG exhibited markedly stronger and more sustained fluorescence signals localized at the tumor sites compared to free ICG, which rapidly dissipated and showed diffuse distribution. Imaging of excised tumors and major organs further confirmed enhanced tumor accumulation and retention of LDH-ICG, indicating that the LDH platform facilitates effective *in vivo* delivery and tumor enrichment.

Direct visual comparison of excised tumors at the end of the treatment period provided intuitive evidence of tumor suppression (Fig. 8C). Tumors from the LDH-YM155 group appeared visibly smaller than those from PBS or LDH groups. Quantitative tumor volume measurements supported this observation. As shown in Fig. 8D, tumor growth in the LDH-YM155 group was significantly inhibited, with final average volumes of ~55 mm^3 on day 14, compared to ~98 mm^3 and ~184 mm^3 in the LDH and PBS groups, respectively. Tumor growth inhibition (TGI) reached approximately 69.75% for LDH-YM155, whereas LDH alone yielded ~46.76% inhibition (Fig. 8F). Tumor weight analysis post-sacrifice also revealed substantial reduction in the LDH-YM155 group, with average tumor mass nearly halved compared to controls (Fig. 8E).

Histopathological and molecular analyses of tumor tissues were conducted to further investigate the therapeutic mechanism. Hematoxylin and eosin (H&E) staining revealed widespread necrosis and loss of tumor cell integrity in the LDH-YM155 group, in contrast to the dense and viable tumor cell morphology observed in the PBS and LDH groups (Fig. 8G, top row). Immunohistochemical staining for Ki-67, a marker of cellular proliferation, showed significantly reduced nuclear staining in the LDH-YM155 group, indicating suppression of tumor cell proliferation (Fig. 8G, middle row). In parallel, TUNEL staining, which labels DNA fragmentation associated with apoptosis, showed markedly higher signal intensity in the LDH-YM155–treated tumors (Fig. 8G, bottom row), demonstrating an increased apoptotic index. Together, these results demonstrate that LDH-YM155 effectively inhibits Hepa1-6 tumor growth and promotes tumor cell death *in vivo*.

3.8 LDH-YM155 activates PANoptosis-associated DAMP signaling and remodels the tumor immune microenvironment in vivo

After confirming the antitumor efficacy of LDH-YM155, we further examined whether treatment induced PANoptosis- and ICD-associated signaling within tumor tissues. Immunofluorescence staining showed increased NLRP3 expression in tumors from the LDH-YM155 group compared with the control and LDH groups, and quantitative analysis confirmed a significant elevation in NLRP3 fluorescence intensity (Fig. 8H and I). RIPK3 staining showed a similar pattern, with stronger RIPK3 signals and increased MFI in LDH-YM155-treated tumors (Fig. 8J and K). These results indicate that LDH-YM155 activates inflammatory cell death-associated signaling *in vivo*.

We next assessed ICD-related DAMP signals in tumor tissues. CRT staining was enhanced in the LDH-YM155 group, indicating increased CRT exposure or accumulation in treated tumors (Fig. 8L and M). In contrast, HMGB1 staining intensity was reduced after LDH-YM155 treatment (Fig. 8N and O), consistent with HMGB1 release from tumor cells during ICD-associated cell death. Together with the *in vitro* extracellular HMGB1 and ATP release results, these *in vivo* staining data further support the induction of ICD-associated DAMP signaling by LDH-YM155.

To determine whether these changes were accompanied by immune microenvironment remodeling, tumor-infiltrating immune cell populations were analyzed by immunofluorescence staining. CD80/CD86 staining showed an increased proportion of $CD80^+CD86^+$ cells in the LDH-YM155 group, indicating enhanced dendritic cell maturation within the tumor microenvironment (Fig. 8P). Macrophage polarization was then evaluated by CD86 and CD206 staining. LDH-YM155 treatment increased $CD86^+$ macrophage-associated signals while reducing $CD206^+$ signals, suggesting a shift from an immunosuppressive M2-like phenotype toward a pro-inflammatory M1-like phenotype (Fig. 8Q).

T-cell infiltration and cytotoxic activation were further assessed by CD4, CD8, and Granzyme B staining. Compared with the control and LDH groups, LDH-YM155-treated tumors showed increased CD8 and Granzyme B signals, indicating enhanced cytotoxic T-cell activation. In contrast, CD4-associated signals were reduced in the LDH-YM155 group (Fig. 8R). These findings suggest that LDH-YM155 reshapes the tumor immune microenvironment toward a more immunostimulatory and antitumor state.

Collectively, LDH-YM155 not only suppresses tumor growth *in vivo* but also activates PANoptosis-associated inflammatory signaling, promotes ICD-related DAMP responses, enhances dendritic cell maturation, shifts macrophage polarization toward a pro-inflammatory phenotype, and increases cytotoxic $CD8^+$Granzyme B^+ T-cell activation in tumor tissues.

3.9 Biosafety evaluation of LDH-YM155 in vivo and in vitro

To evaluate the biosafety of the LDH-YM155 nanocomposite, hemolysis assays, body weight monitoring, and histopathological examination of major organs were performed.

A hemolysis assay was conducted to assess the potential membrane-disruptive effects of LDH and LDH-YM155 on red blood cells. As shown in Fig. 9A, neither LDH nor LDH-YM155 caused detectable hemolysis across a wide concentration range (25–400 μg mL^{-1}), with hemolysis ratios consistently below 2%. In contrast, the positive control (double-distilled water) resulted in complete hemolysis, confirming assay validity. These results indicate that both formulations exhibit good hemocompatibility and do not cause acute membrane damage to erythrocytes *in vitro*.

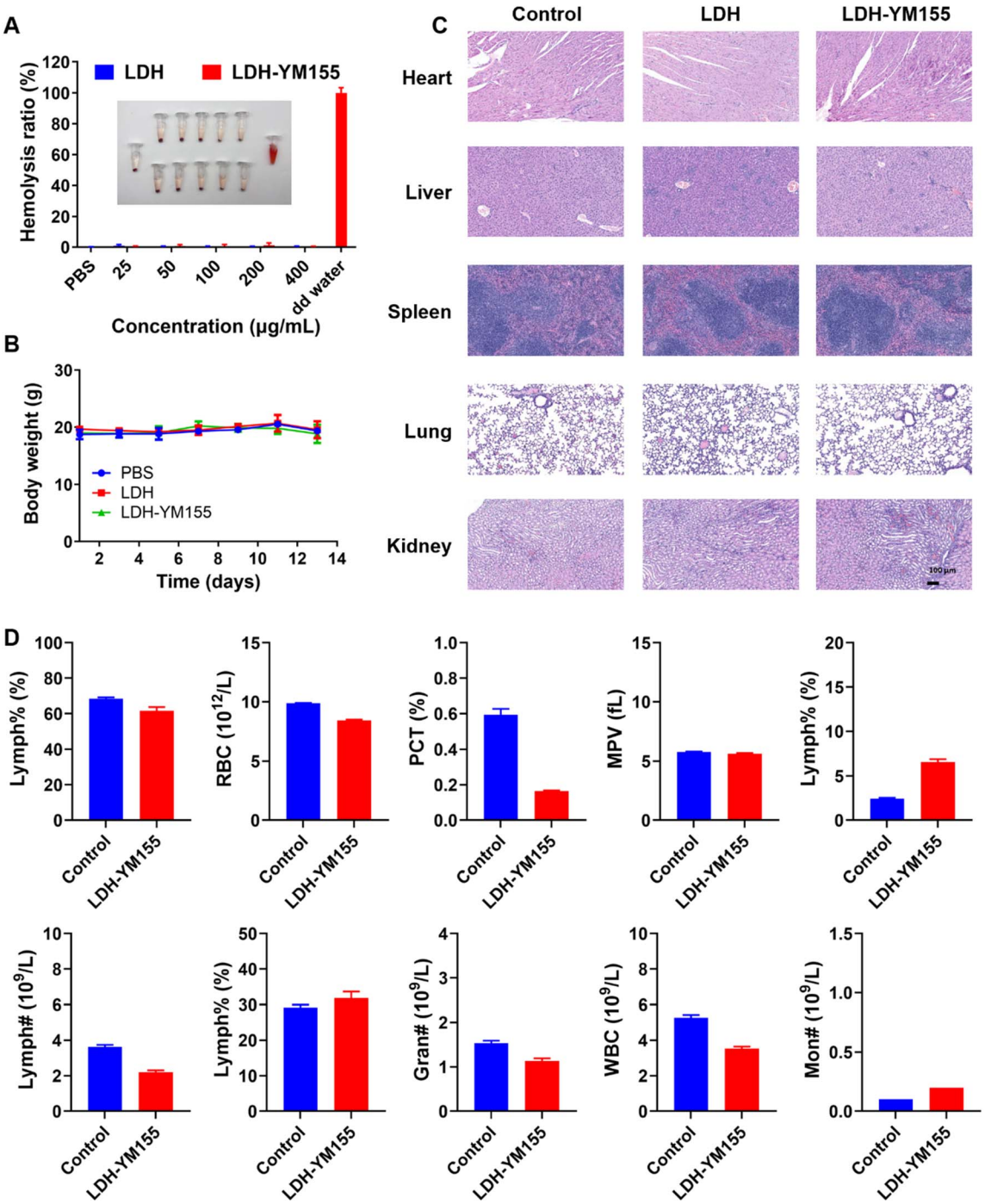

Fig. 9 Evaluation of the *in vivo* biosafety profile of LDH-YM155. (A) Hemolytic activity of red blood cells following incubation with increasing concentrations of LDH or LDH-YM155 (25–400 μg mL^{-1}), with double-distilled water used as the positive control. Representative photographs of hemolysis samples are shown in the inset. (B) Changes in body weight of mice during the 14 day treatment period ($n = 5$). (C) Representative H&E-stained sections of major organs from mice treated with PBS, LDH, or LDH–YM155. Scale bar: 100 μm. (D) Routine blood analysis after treatment. Data are presented as mean ± SD, $n = 3$. Scale bar: 100 μm.

During the 14 day treatment period in tumor-bearing mice, body weight was recorded as an indirect indicator of systemic toxicity. As illustrated in Fig. 9B, no significant loss of body weight was observed in any treatment group (PBS, LDH, or LDH-YM155), with weights remaining stable around 20–22 g throughout the study. This suggests that repeated intravenous administration of LDH-YM155 did not elicit apparent systemic toxicity or impair general health status.

To further assess long-term biosafety, histological analyses of major organs were performed 14 days post-treatment using H&E staining (Fig. 9C). Tissue sections from the LDH-YM155 group displayed normal morphology comparable to PBS and

LDH groups, with no evident signs of inflammation, necrosis, fibrosis, or structural damage in any organ examined. Cardiac fibers were intact, hepatic lobules were well organized, splenic architecture remained preserved, alveolar structure was unaltered, and renal glomeruli and tubules showed no pathological abnormalities.

Routine blood analysis was further performed to quantitatively evaluate systemic hematological safety. Major hematological parameters, including lymphocyte percentage, red blood cell count, hematocrit, mean platelet volume, lymphocyte count, granulocyte count, white blood cell count, and monocyte count, showed no obvious abnormalities after LDH-YM155 treatment compared with the control group (Fig. 9D). These results indicate that LDH-YM155 did not induce apparent hematological toxicity under the tested treatment conditions.

Together, these results confirm that the LDH-YM155 nanocomposite exhibits favorable *in vitro* hemocompatibility, induces no significant body weight fluctuation, and causes no detectable histological toxicity to major organs *in vivo*, supporting its biocompatibility for biomedical applications.

4 Conclusions

In this study, we developed LDH-YM155, a MgAl-layered double hydroxide nanosheet-based nanocomposite, to improve the delivery efficiency and therapeutic performance of the Survivin inhibitor YM155 for hepatocellular carcinoma treatment. LDH-YM155 exhibited favorable physicochemical stability, pH-responsive YM155 release, efficient cellular internalization, and stronger cytotoxicity than free YM155. Its antitumor activity was observed in both Hepa1-6 and SK-Hep1 cells and was accompanied by time- and dose-dependent Survivin suppression, mitochondrial ROS accumulation, mitochondrial dysfunction, and Cytochrome *c* release.

Mechanistically, LDH-YM155 induced PANoptosis in Hepa1-6 cells, as supported by inhibitor-rescue experiments and the coordinated activation of apoptotic, inflammasome-associated pyroptotic, and necroptotic signaling pathways, including caspase-3/8 activation, NLRP3/ASC/caspase-1 signaling, and RIPK3/p-MLKL activation. In parallel, LDH-YM155 promoted immunogenic cell death-associated DAMP signaling, as evidenced by surface CRT exposure, extracellular HMGB1 and ATP release, and increased LDH release. Conditioned medium from LDH-YM155-treated tumor cells further promoted dendritic cell maturation, indicating that LDH-YM155-induced tumor cell death generated functional immunostimulatory signals.

Transcriptomic profiling further supported the activation of inflammatory and cell death-related signaling pathways, consistent with the experimental findings. *In vivo*, LDH-YM155 accumulated in tumor tissues, significantly inhibited Hepa1-6 tumor growth, reduced Ki-67 expression, and increased TUNEL-positive tumor cell death. Immunofluorescence analysis of tumor tissues further confirmed the activation of PANoptosis- and ICD-associated signals, enhanced dendritic cell maturation, macrophage polarization toward a pro-inflammatory phenotype, and increased cytotoxic $CD8^{+}$ Granzyme B^{+} T-cell activation. In addition, biosafety evaluation demonstrated good hemocompatibility, stable body weight, no obvious histological damage in major organs, and no marked abnormalities in routine blood parameters.

Collectively, these findings demonstrate that LDH-based delivery enhances the antitumor efficacy of YM155 and redirects tumor cell death toward a PANoptosis-associated and immunogenic phenotype. This process further remodels the tumor immune microenvironment toward an antitumor state, highlighting LDH-YM155 as a promising nanotherapeutic strategy for hepatocellular carcinoma treatment.

Conflicts of interest

The authors declare that they have no known competing financial interests or personal relationships that could have appeared to influence the work reported in this paper.

Data availability

The transcriptomics data reported in this paper have been deposited in the OMIX, China National Center for Bioinformation/Beijing Institute of Genomics, Chinese Academy of Sciences (https://ngdc.cncb.ac.cn/omix: accession no. OMIX015215).

Acknowledgements

This work was supported by the Chongqing Technology Innovation and Application Development Special Key Project (No. CSTB2022TIAD-KPX0170) and the Chongqing Science and Health Joint Medical Research Major Project (No. 2024DBXM003).

Notes and references

1 F. Bray, M. Laversanne, H. Sung, J. Ferlay, R. L. Siegel, I. Soerjomataram and A. Jemal, Global cancer statistics 2022: GLOBOCAN estimates of incidence and mortality worldwide for 36 cancers in 185 countries, *Ca-Cancer J. Clin.*, 2024, **74**(3), 229–263.

2 Q. Li, C. Ding, M. Cao, F. Yang, *et al.*, Global epidemiology of liver cancer 2022: An emphasis on geographic disparities, *Chin. Med. J.*, 2024, **137**(19), 2334–2342.

3 J. M. Llovet, R. K. Kelley, A. Villanueva, *et al.*, Hepatocellular carcinoma, *Nat. Rev. Dis. Primers*, 2021, **7**(1), 6.

4 A. G. Singal, *et al.*, AASLD Practice Guidance on prevention, diagnosis, and treatment of hepatocellular carcinoma, *Hepatology*, 2023, **78**(6), 1922–1965.

5 B. Sangro, *et al.*, EASL clinical practice guidelines on the management of hepatocellular carcinoma, *J. Hepatol.*, 2025, **82**(2), 315–374.

6 M. Reig, A. Forner, J. Rimola, *et al.*, BCLC strategy for prognosis prediction and treatment recommendation: The 2022 update, *J. Hepatol.*, 2022, **76**(3), 681–693.

7 X. Wu, *et al.*, Programmed cell death in hepatocellular carcinoma: mechanisms and therapeutic prospects, *Cell Death Discov.*, 2024, **10**, 356.

8 Q. Wang and M. I. Greene, Survivin as a therapeutic target for the treatment of human cancer, *Cancers*, 2024, **16**(9), 1705.
9 G. Vader, R. H. Medema and S. M. A. Lens, Survivin mediates targeting of the chromosomal passenger complex to the centromere and midbody, *EMBO Rep.*, 2006, **7**(1), 85–92.
10 G. Siragusa, *et al.*, Survivin (BIRC5): Implications in cancer therapy, *Life Sci.*, 2024, **350**, 122788.
11 R. J. Kelly, A. Lopez-Chavez, D. Citrin, J. E. Janik and J. C. Morris, Impacting tumor cell-fate by targeting the inhibitor of apoptosis protein survivin, *Mol. Cancer*, 2011, **10**, 35.
12 Y. Liu, *et al.*, Identification and validation of Birc5 as a novel activated cell cycle program biomarker associated with infiltration of immunosuppressive myeloid-derived suppressor cells in hepatocellular carcinoma, *Cancer Med.*, 2023, **12**(15), 16370–16385.
13 Y. Mai, *et al.*, BIRC5 knockdown ameliorates hepatocellular carcinoma progression via regulating PPARγ pathway and cuproptosis, *Discov. Oncol.*, 2024, **15**, 706.
14 J.-T. Chiou, *et al.*, Inhibition of Sp1-mediated survivin and MCL1 expression cooperates with SLC35F2 and myeloperoxidase to modulate YM155 cytotoxicity to human leukemia cells, *Biochem. Pharmacol.*, 2021, **188**, 114544.
15 T. J. West, *et al.*, A cell type selective YM155 prodrug targets receptor-interacting protein kinase 2 to induce brain cancer cell death, *J. Am. Chem. Soc.*, 2023, **145**(15), 8355–8363.
16 H. A. Kenny, *et al.*, Navitoclax, a Bcl-2/xl inhibitor, and YM155, a survivin inhibitor, in combination with carboplatin, effectively inhibit ovarian cancer tumor growth, *Mol. Cancer Ther.*, 2025, **24**(8), 1252–1264.
17 X. Jin, *et al.*, YM155 exerts anti-myeloma effects via Myc/BBC3 signaling pathway in vitro, *Blood*, 2024, **144**, 6849.
18 Y. Voges, *et al.*, Effects of YM155 on survivin levels and viability in neuroblastoma cells with acquired drug resistance, *Cell Death Dis.*, 2016, **7**, 2410.
19 H. Kalkavan, S. Rühl, J. J. P. Shaw and D. R. Green, Non-lethal outcomes of engaging regulated cell death pathways in cancer, *Nat. Cancer*, 2023, **4**, 795–806.
20 X. Jin, W. Jin, L. Tong, J. Zhao, L. Zhang and N. Lin, Therapeutic strategies of targeting non-apoptotic regulated cell death (RCD) with small-molecule compounds in cancer, *Acta Pharm. Sin. B*, 2024, **14**(7), 2815–2853.
21 G. Hou, Y. Chen, H. Lei, S. Lu and L. Cheng, Nanomaterials-Induced PANoptosis: A Promising Anti-Tumor Strategy, *Angew. Chem., Int. Ed.*, 2025, **64**(5), e202419649.
22 J.-F. Lin, T.-T. Wang, R.-Z. Huang, Y.-T. Tan, D.-L. Chen and H.-Q. Ju, PANoptosis in cancer: bridging molecular mechanisms to therapeutic innovations, *Cell. Mol. Immunol.*, 2025, **22**, 996–1011.
23 G. Zhu, Y. Qian, M. Gao, Q. Sun, P. Ma, J. Lin and C. Li, A novel nano-biocomposite synergistically activates PANoptosis and cGAS-STING for precise cancer immunotherapy, *Biomaterials*, 2026, **327**, 123758.
24 H. You, *et al.*, Cell death shapes cancer immunity: spotlighting PANoptosis, *J. Exp. Clin. Cancer Res.*, 2024, **43**, 168.
25 G. Kroemer, C. Galassi, L. Zitvogel and L. Galluzzi, Immunogenic cell stress and death, *Nat. Immunol.*, 2022, **23**, 487–500.
26 R. Chen, J. Zou, J. Liu, R. Kang and D. Tang, DAMPs in the immunogenicity of cell death, *Mol. Cell*, 2025, **85**(20), 3874–3889.
27 M. Fang, J. Zheng, Q. Song, J. Huang, R. Cao, P. Li, Y. Chen and L. Zhang, Breaking Apoptosis-Induced Immune Silence: Ultrasound-Activated Nano-Oncolytic Therapy Reinvigorates Antitumor Immunity, *Adv. Mater.*, 2025, **37**(35), 2508681.
28 M. S. Khan, *et al.*, Advances in PLGA-based polymeric nanocarriers for colorectal cancer therapy: overcoming chemoresistance through controlled delivery strategies, *Mol. Cancer*, 2025, **24**(1), 288.
29 C. Zhu, J. Jiang, Y. Jia, *et al.*, Beyond drug delivery system: immunomodulatory layered double hydroxide nanoadjuvants take an essential step forward in cancer immunotherapy, *Acc. Mater. Res.*, 2023, **4**(9), 758–771.
30 V. K. A. Shirin, *et al.*, Advanced drug delivery applications of layered double hydroxides, *J. Controlled Release*, 2021, **330**, 398–426.
31 L. Li, *et al.*, Layered double hydroxides: recent progress and promising perspectives toward biomedical applications, *Adv. Sci.*, 2024, **11**(20), 2306035.
32 M. T. Shivakumar, *et al.*, Layered double hydroxides-based nanomaterials: recent advances in drug delivery and biomedical applications, *Health Nanotechnol.*, 2025, **1**, 18.
33 D.-H. Park, *et al.*, Biodegradable inorganic nanovector: passive versus active tumor targeting in siRNA transportation, *Angew Chem. Int. Ed. Engl.*, 2016, **55**(14), 4582–4586.
34 J. Luo, *et al.*, Layered double hydroxides for regenerative nanomedicine and tissue engineering: recent advances and future perspectives, *J. Nanobiotechnol.*, 2025, **23**, 370.
35 S. Senapati, *et al.*, Layered double hydroxide nanoparticles for efficient gene delivery, *Bioconjug. Chem.*, 2019, **30**(10), 2544–2554.
36 N. M. Mohamed, *et al.*, A comprehensive review and in silico analysis of the role of survivin (BIRC5) in hepatocellular carcinoma hallmarks: A step toward precision, *Int. J. Biol. Macromol.*, 2025, **311**, 143616.